Division of

Engineering Research

and Development
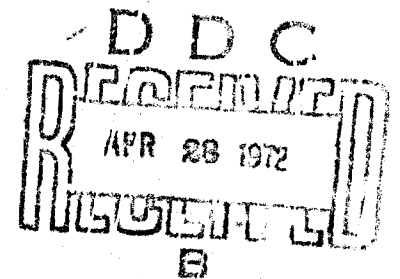
UNIVERSITY OF RHODE ISLAND

COLLEGE OF ENGINEERING   KINGSTON, RHODE ISLAND 02881

Prepared under Contract No. N00019 71 C 0244

for

NAVAL AIR SYSTEMS COMMAND

DEPARTMENT OF THE NAVY

WASHINGTON, D.C. 20360

by

UNIVERSITY OF RHODE ISLAND

KINGSTON, RHODE ISLAND 02881

Final Technical Report
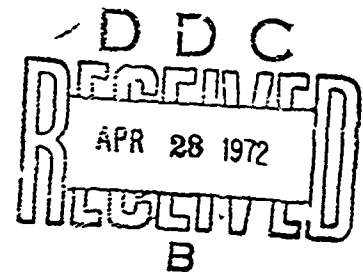
15 November 1970 - 15 November 1971

December 1971

DYNAMIC AND THERMAL ASPECTS

OF

CERAMIC PROCESSING

P. J. GIELISSE

T. J. KIM

A. CHOUDRY

DOCUMENT CONTROL DATA - R & D

Security classification of title, body of abstract and indexing annotation must be entered when the overall report is classified

1 ORIGINATING ACTIVITY (Corporate author)	2a. REPORT SECURITY CLASSIFICATION
University of Rhode Island Kingston, Rhode Island	Unclassified
	2b. GROUP

3 REPORT TITLE

Dynamic and Thermal Aspects of Ceramic Processing

4 DESCRIPTIVE NOTES (Type of report and inclusive dates)

Final Technical Report November 15, 1970 to November 15, 1971

5 AUTHOR(S) (First name, middle initial, last name)

Peter J. Gielisse, T.J. Kim and A. Choudry

6 REPORT DATE	7a. TOTAL NO OF PAGES	7b. NO OF REFS
15 December 1971	101	9
8a CONTRACT OR GRANT NO. N00019 71 C 0244	9a. ORIGINATOR'S REPORT NUMBER(S)	
b. PROJECT NO 98-04-4042		
c.	9b. OTHER REPORT NO(S) (Any other numbers that may be assigned this report)	
d.		

10 DISTRIBUTION STATEMENT

This document has been approved for public release and sale; its distribution is unlimited.

11 SUPPLEMENTARY NOTES	12 SPONSORING MILITARY ACTIVITY
None	Naval Air Systems Command Department of the Navy Washington, D.C. 20360

13 ABSTRACT

It has been shown that with wheelspeed increasing, grinding forces on ceramics initially drop sharply, pass through a minimum and then slowly rise again. This behavior has been explained by a proposed dynamic elastic grinding model. It has further been possible to obtain information on actual volume of material removal as a function of wheelspeed. Both the depth to which material is removed and width of the groove are substantially larger than geometric considerations would indicate. Both parameters increase significantly with increase in speed.

A new piezoelectric dynamometer has been designed which enabled study of the impulse of individual cutting events.

High speed photography and photocell synchronized flash photography have made the cutting event visible and data support evidence from other indirect methods.

Quantitative data on wear of the diamond is presented and supported with Scanning Electron Micrographs. Two types of failure occur: cratering and gradual wear.

Our initial phenomenological grinding model has been extended and a dynamic-elastic grinding model is presented.

DD FORM 1473 (PAGE 1)
1 NOV 65

KEY WORDS	LINK A		LINK B		LINK C	
	ROLE	WT	ROLE	WT	ROLE	WT

DD FORM 1473 (BACK)

(PAGE 2)

DYNAMIC AND THERMAL ASPECTS
OF
CERAMIC PROCESSING

P. J. GIELISSE

T. J. KIM

A. CHOUDRY

UNIVERSITY OF RHODE ISLAND

KINGSTON, RHODE ISLAND 02881

PREFACE

The work reported here was carried out by the University of Rhode Island under Contract No. N00019 71 C 0244 with the Naval Air Systems Command, Department of the Navy, Washington, D.C. This project is monitored for the Naval Air Systems Command by Mr. Charles F. Bersch.

The report covers work done between 15 November, 1970 and 15 November, 1971. The principal investigators were Peter J. Gielisse and T. J. Kim. Contributions were also made by J. Stanislao, a previous investigator who left the University of Rhode Island to take up the position of Chairman, Department of Industrial Engineering, Cleveland State University in June 1971, and A. Choudry of the Physics Department of the University of Rhode Island.

Manuscript released by the authors for publication as a Final Technical Report, December 1971.

Approved for
University of Rhode Island

L. D. Conta

L. D. Conta
Director, Division of Research and Development
Dean, College of Engineering

15 December 1971

TABLE OF CONTENTS

ILLUSTRATIONS

TABLES

ABSTRACT

It has been shown that with wheelspeed increasing, grinding forces on ceramics initially drop sharply, pass through a minimum and then slowly rise again. This behavior has been explained by a proposed dynamic elastic grinding model. It has further been possible to obtain information on actual volume of material removal as a function of wheelspeed. Both the depth to which material is removed and width of the groove are substantially larger than geometric considerations would indicate. Both parameters increase significantly with increase in speed.

A new piezoelectric dynamometer has been designed which enabled study of the impulse of individual cutting events.

High speed photography and photocell synchronized flash photography have made the cutting event visible and data support evidence from other indirect methods.

Quantitative data on wear of the diamond is presented and supported with Scanning Electron Micrographs. Two types of failure occur: cratering and gradual wear.

Our initial phenomenological grinding model has been extended and a dynamic-elastic grinding model is presented.

I GRINDING FORCES AT HIGH SPEED

A. EXPERIMENTAL

Force behavior as a function of wheelspeed has previously been
reported up to relatively low speeds, reflecting conventional grinding
practices.[1,2] Force levels generally sharply decrease with increasing wheel
speed and tend to assymptotic behavior. It was felt desirable to extend
measurements to appreciably higher speed regimes to verify this type of
behavior or to determine possible deviations. We have made use of a high
speed grinder capable of shaft revolutions up to 25,000 rpm which was
fitted with a two and one-half inch diameter wheel carrying the diamond in
a special holder on its periphery. Increasing the surface speed by increasing
the diameter of the wheel beyond this diameter is not warranted because of
spindle deflection and safety considerations.

Accurate recording of the absolute force levels at these high
speeds initially met with considerable difficulty, that is to say with
the force recording equipment we had previously used. It was found that,
due to the very low force levels at high speeds the dynamometer sensitivity
had to be increased. This was initially attempted by providing two extra
strain gauges, in series, in the bridges for both normal and tangential
force measurements through which the output signal was increased. In addition,
the thickness of the octagonal rings, the deflecting elements of the strain

gauge type dynamometer, had to be reduced to a mere 1/32 of an inch. In this manner sensitivity and signal level were adjusted properly for the high speed range (> 10,000 rpm). Severe resonance problems resulted, however, in the low speed range (> 10,000 rpm) due to the greatly reduced rigidity of the dynamometer coupled with the much higher forces generated. These problems were overcome by casting wax rings in the circular cutouts of the octagonal memebers and adjusting rigidity by progressively removing more and more wax (by slotting the wax rings) at higher speed ranges. The dynamometer had to be separately calibrated for each configuration and hence speed range over which it was usable.

It was further found that several correction factors had to be used to generate the actual force levels from those recorded initially. A certain time is required for the dynamometer to achieve full deflection and to regain its initial state depending on the rigidity of the system. If the time between two cuts is too small to record full force and regain the initial state, the force record will show a steadily increasing force as a function of time, until a steady state is reached. A second correction factor was needed to compensate for the difference between the cutting time and the response time of the recorder. If the actual time per individual cut is less than the recorder response time, as was the case with the equipment used, the recorder will not indicate the full input but only a percentage of the actual force. Correction factors, representing the ratio of actual cutting time for each cut to the response time of the recorder, were used to calculate real force levels.

The pertinent data for the conditions of our experiments are
shown for reference purposes in Table I. As a result, two sets of data
are given in Figure 1 which shows the force behavior as a function of
speed up to 25,000 rpm. Extreme caution should therefore be exercised in
interpreting grinding force data obtained with strain gauge type dyna-
mometers and low response type recorders. This type of problem can be
overcome through the use of high sensitivity fast response dynamometers
which are so designed as to overcome resonance problems, i.e. are applicable
over the entire desired speed range. Such a design is described in
Section II and is the type of instrument presently in use in our laboratory.
It was felt important to advance the background given above both for purposes
of possible benefit to other investigators as well as to document the
manner in which the significant data of subsection II B were obtained.

B. ANALYSIS IN TERMS OF MATERIAL REMOVAL

It had been noted earlier, through microscopic and SEM analysis,
that the actual width of the groove "cut" is considerably larger than
that corresponding to the geometric width as a result of depth of cut and
diamond cone angle. Routine microscopic observations of all grooves indicated
a similar behavior with reference to groove depth with a possible dependence
on wheelspeed. A full analysis of actual width and depth of the groove as a
function of wheelspeed (up to 20,000 rpm) had led to some surprising results
both in terms of the actual amount of material removed as well as its
dependence on wheelspeed.

TABLE I

PERTINENT SYSTEMS PARAMETERS USED IN MAKING DYNAMOMETER-RESPONSE AND RECORDING CORRECTIONS

Wheel Velocity	Depth of Cut	Angular Velocity	Sweep Angle	Cutting Time	Wheel Revolution Time	Non-Cutting Time	Δt for Steady State	Number of Cuts in Δt	Total Input Time	Input Recorded
R.P.M.	Inches	Rad/Sec	Degrees	Msec	Sec	Msec (approx)	Sec	---	Msec	%
2,000	.003	209.4	7.766°	0.6460	.03	30	0.10	3.3	2.13	42.6
5,000	.003	523.80	7.766°	0.2708	0.012	12	0.15	12.5	3.38	67.5
10,000	.003	1047.6	7.766°	0.1354	0.006	6	0.15	25	3.39	67.8
15,000	.003	1571.4	7.766°	0.0903	0.004	4	0.15	37.5	3.38	67.5
20,000	.003	2094.4	7.766°	0.0646	0.003	3	0.175	58.3	3.78	75.4
25,000	.003	2619.0	7.766°	0.0542	0.0024	2.4	0.333	138.5	7.5	100
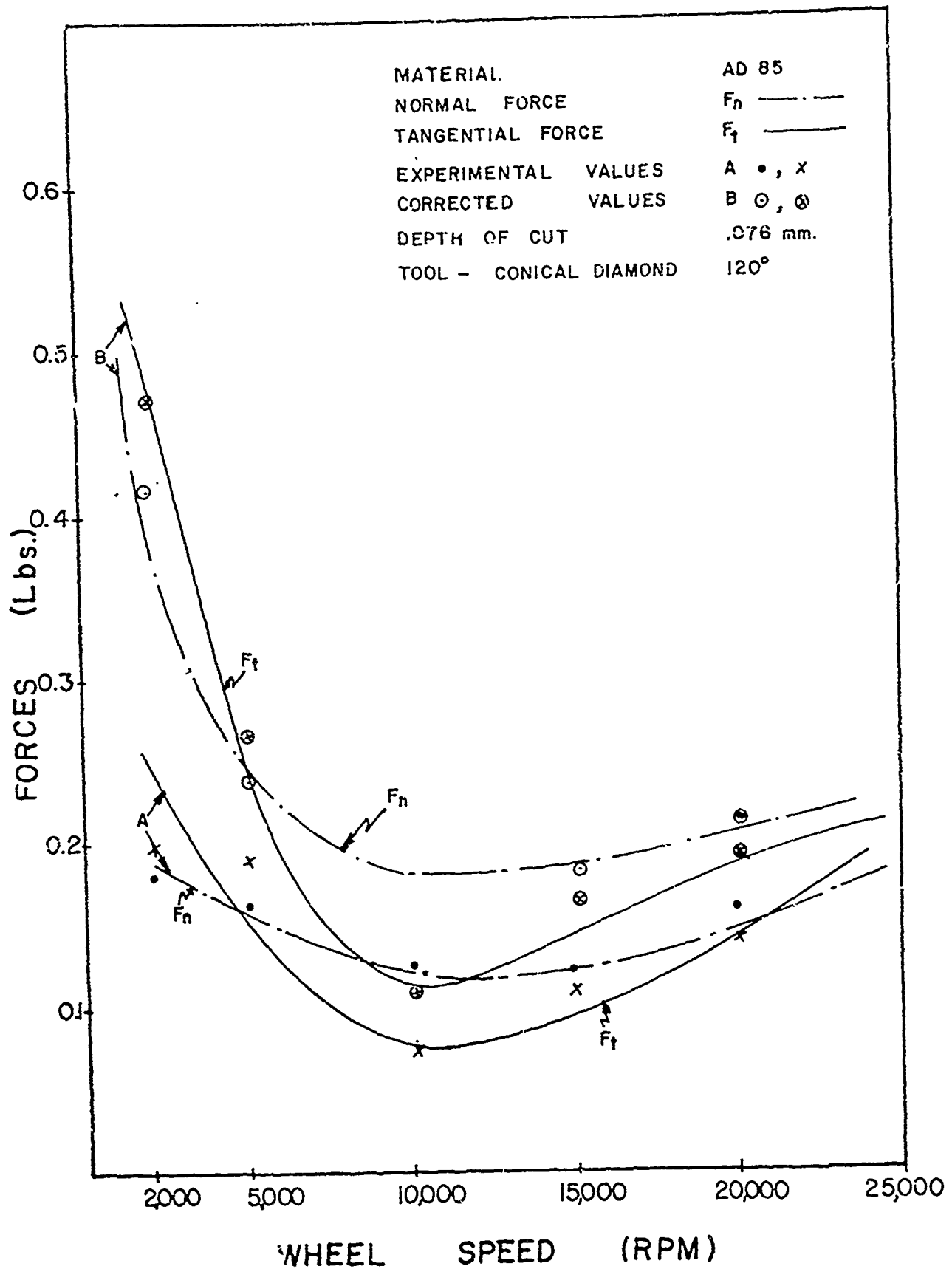
FIGURE 1. Peak Grinding Forces as a Function of Wheelspeed Before and After Adjustments for Dynamometer and Electronic Response. AD 85, .003" Depth of Cut, 120° Diamond Cone.

TABLE II

MEASUREMENTS OF ACTUAL DEPTH OF GROOVE (MM)
AS A FUNCTION OF WHEELSPEED FOR AD 85, .003" DEPTH OF CUT,
120° DIAMOND CONE, DYNAMOMETER MOUNTED

Position #	Wheelspeed (rpm)					
	25,000	20,000	15,000	10,000	5,000	2,000
1	.170	.140	.104	.094	.078	.072
2	.170	.130	.120	.090	.084	.090
3	.164	.132	.120	.096	.080	.084
4	.160	.138	.116	.096	.086	.110
5	.172	.124	.104	.098	.092	.100
6	.160	.134	.108	.094	.088	.084
7	.150	.138	.098	.088	.068	.120
8	.152	.140	.104	.090	.072	.092
9	.174	.138	.106	.108	.078	.088
10	.170	.130	.100	.098	.068	.100
11	.180	.136	.120	.096	.084	.064
12	.164	.138	.118	.090	.090	.106
13	.160	.144	.122	.088	.082	.120
14	.148	.134	.116	.092	.080	.150
15	.160	.140	.118	.096	.078	.114
Average	0.1636	0.1356	0.1116	0.0944	0.0804	0.1008

TABLE III

MEASUREMENTS OF ACTUAL DEPTH OF GROOVE (MM)

AS A FUNCTION OF WHEELSPEED FOR AD 85, .003" DEPTH OF CUT,

120° DIAMOND CONE, BLOCK MOUNTED

Position #	Wheelspeed (rpm)					
	25,000	20,000	15,000	10,000	5,000	2,000
1	.160	.134	.108	.096	.090	.084
2	.166	.120	.108	.098	.076	.100
3	.172	.138	.120	.096	.080	.070
4	.162	.124	.098	.098	.076	.088
5	.168	.128	.104	.090	.074	.100
6	.158	.120	.106	.092	.068	.110
7	.144	.130	.118	.102	.078	.086
8	.148	.110	.120	.106	.072	.118
9	.140	.132	.104	.084	.068	.170
10	.140	.132	.100	.078	.070	.120
11	.168	.134	.106	.098	.078	.130
12	.152	.128	.116	.100	.080	.084
13	.158	.118	.114	.092	.080	.080
14	.154	.124	.116	.090	.070	.070
15	.164	.136	.114	.094	.080	.120
Average	0.1570	0.1272	0.1182	0.0944	0.0760	0.1066

TABLE IV

MEASUREMENTS OF ACTUAL WIDTH OF GROOVE (MM)
AS A FUNCTION OF WHEELSPEED FOR AD 85, 0.003" DEPTH OF CUT,
120° DIAMOND CONE, DYNAMOMETER MOUNTED

Position #	Wheelspeed (rpm)					
	25,000	20,000	15,000	10,000	5,000	2,000
1	.388	.400	.403	.320	.440	.400
2	.555	.403	.505	.340	.360	.500
3	.450	.465	.500	.290	.362	.480
4	.500	.435	.400	.300	.370	.510
5	.460	.432	.360	.390	.400	.504
6	.540	.458	.340	.372	.375	.603
7	.465	.410	.300	.410	.362	.580
8	.560	.430	.370	.360	.280	.455
9	.536	.426	.395	.300	.400	.450
10	.594	.401	.375	.354	.340	.480
Average	0.5049	0.4260	0.3948	0.3436	0.3689	0.4952

TABLE V

MEASUREMENTS OF ACTUAL WIDTH OF GROOVE (MM)
AS A FUNCTION OF WHEELSPEED FOR AD 85, 0.003" DEPTH OF CUT,
120° DIAMOND CONE, BLOCK MOUNTED

Position #	Wheelspeed (rpm)					
	25,000	20,000	15,000	10,000	5,000	2,000
1	.441	.515	.340	.345	.342	.380
2	.540	.388	.320	.350	.300	.450
3	.509	.480	.380	.300	.310	.490
4	.445	.320	.360	.361	.380	.394
5	.405	.510	.359	.314	.372	.448
6	.610	.413	.300	.300	.361	.580
7	.440	.421	.342	.310	.379	.543
8	.510	.380	.412	.304	.314	.398
9	.470	.436	.362	.290	.301	.419
10	.624	.465	.370	.350	.340	.510
Average	0.4997	0.4328	0.3545	0.3224	0.3399	0.4612

All reported results were obtained in cutting AD 85 alumina with a constant depth of cut (0.003 inches) and wheel speeds ranging from 2000-25,000 rpm. The diamond had a cone angle of 120° and was mounted on a two and one-half inch diameter wheel. The actual depth and widths of the grooves were obtained microscopically. An average of 15 observations randomly spaced along the 4 inch length of the ceramic determined the actual depth. Depth was the microscope tube movement required to go from a fully focused position on the top of the workpiece to a focused condition at the deepest point in the groove. Width was similarly determined at ten randomly spaced positions along the length of the workpiece by noting the movement of the microscope stage required to go from one side to the other. Actual readings for both cases are given in Table II through V.

Two types of experiments were conducted. In one case the workpiece was mounted on the dynamometer, in the other case, it was mounted on a very massive aluminum block. This would test whether the depth and width of the grooves were influenced by the dynamometer rigidity or "springiness." As may be seen from the data (Tables II-V) the averages, for both depth and width, for both cases are very close. Only slightly lower readings seem indicated for the block type results. Dynamometer mounting did not significantly influence the results.

Figure 1 in which only the upper set of curves need be considered, shows the force profile as wheelspeed is increased. Forces initially come down sharply, as was previously found. They do not continue to level off
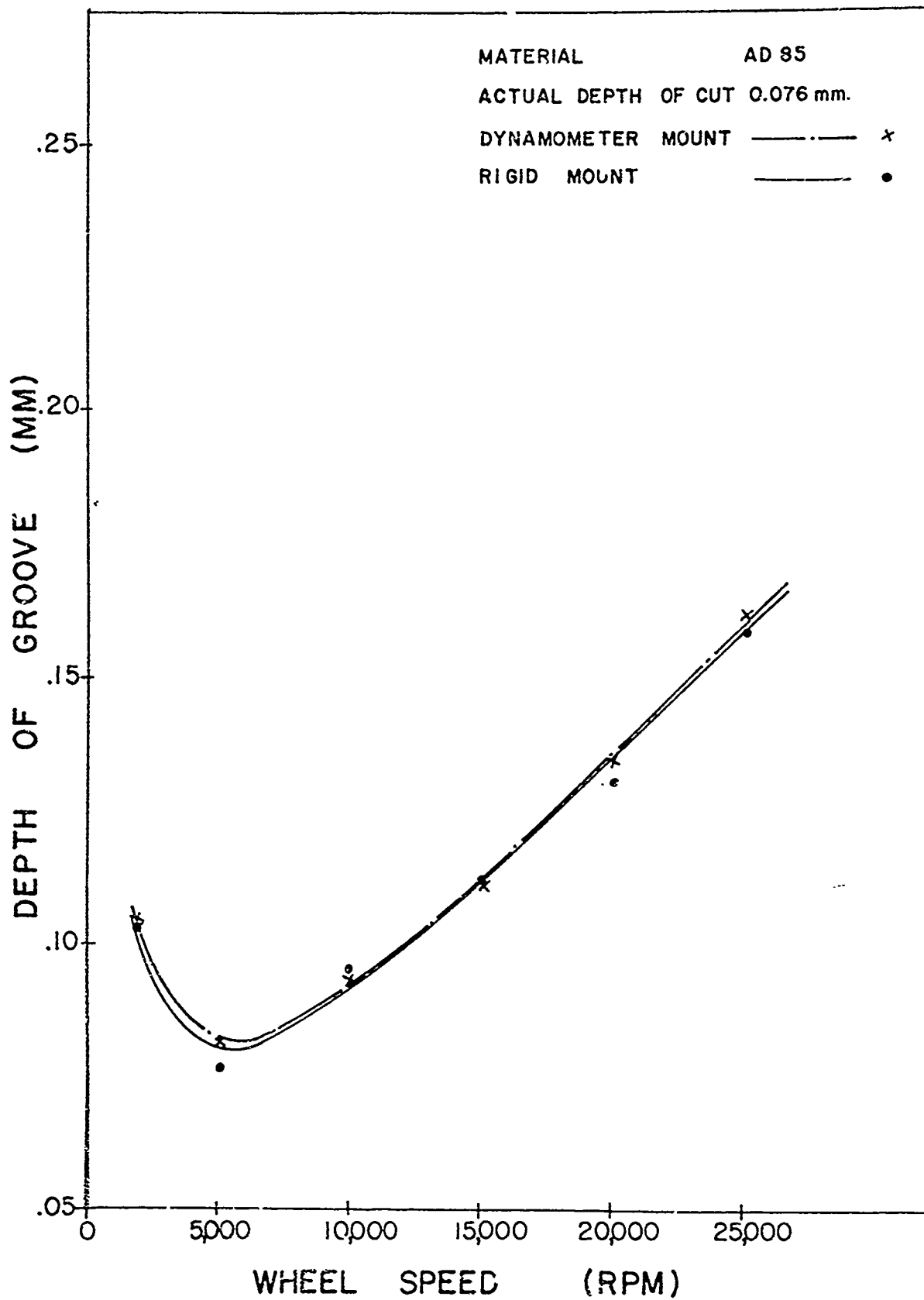
FIGURE 2. Measured Depth of Groove Versus Wheelspeed.
AD 85, .003" Depth of Cut, 120° Diamond Cone.
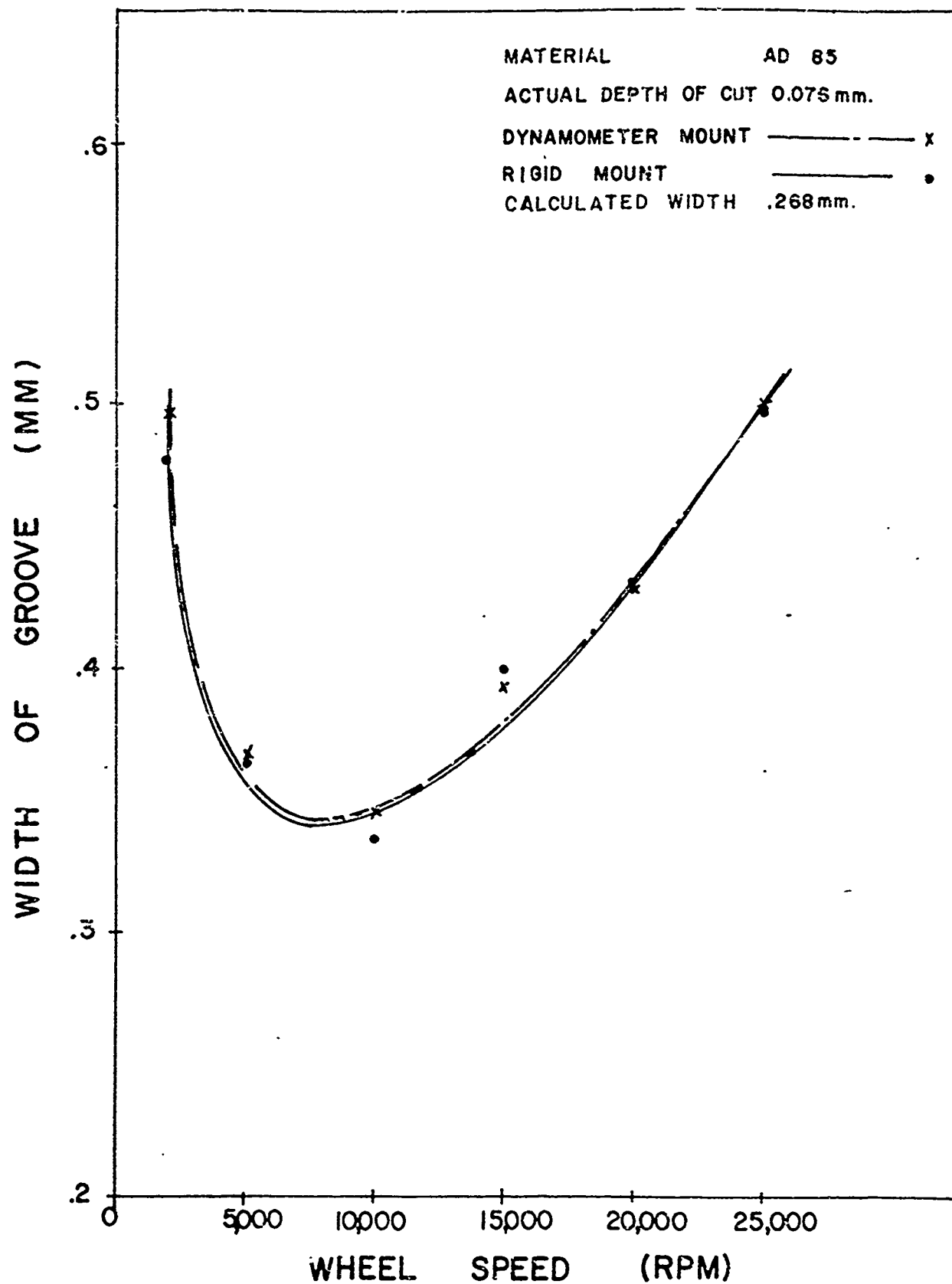
FIGURE 3, Measured Width-of Groove Versus Wheelspeed.
AD 85, .003" Depth of Cut, 120° Diamond Cone.
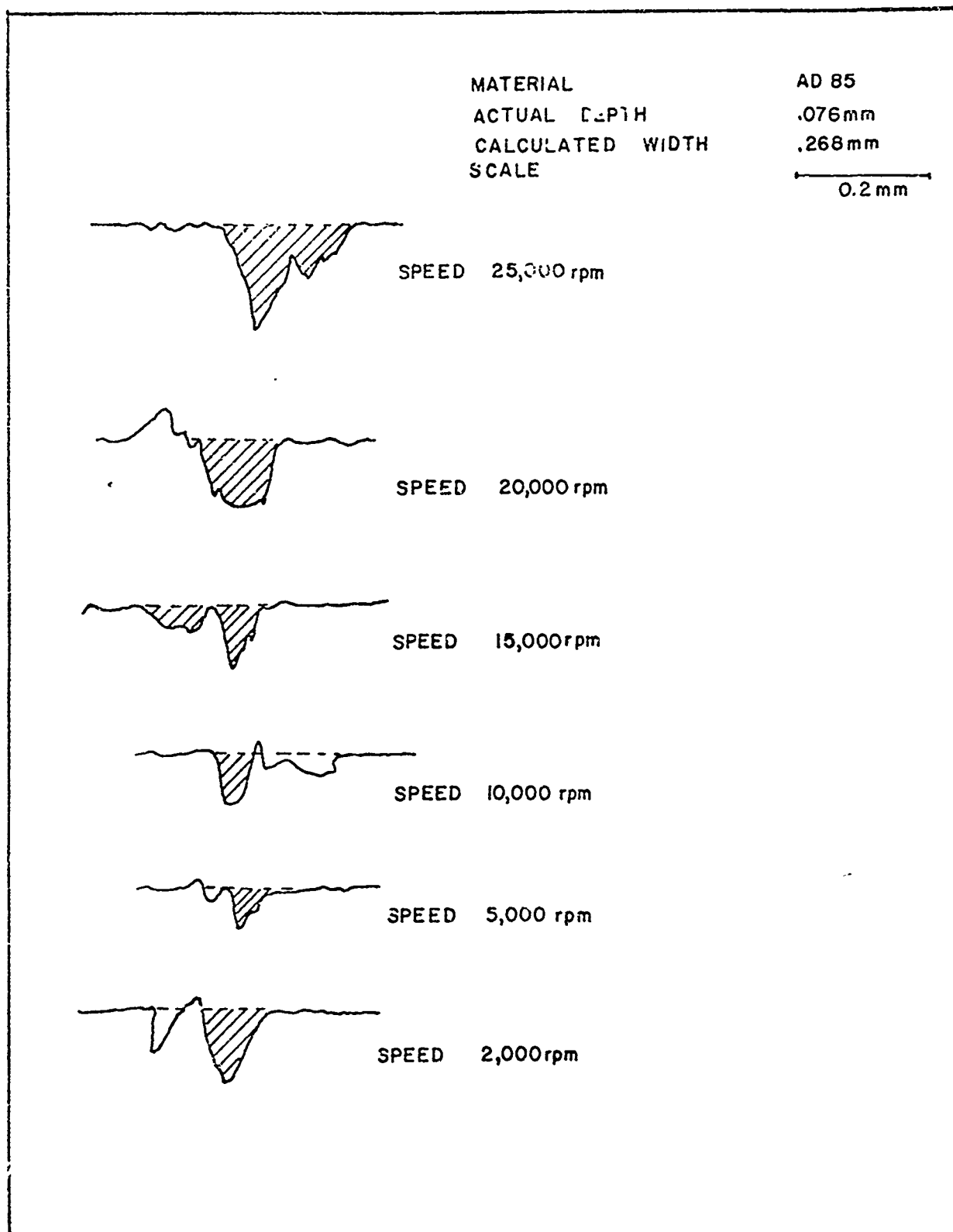
FIGURE 4. Profilometer Traces Recorded at One Point Across a Series of Grooves Cut at Various Wheelspeeds. AD 85, .003" Depth of Cut, 120° Diamond Cone.

but produce a minimum, around 10,000 rpm for AD 85 after which the forces gradually increase again. The reason for this experimental finding may be found in the fundamental principles governing the mode of interaction resulting from high speed cyclic loading of a brittle material as presented in Section V B. The forces do increase after passing through a minimum but not at as high a rate as on the low speed side of the minimum.

The data on actual depth of cut as a function of wheelspeed are shown in Figure 2. Only at the minimum in the curve is the actual depth of cut equal to the geometric depth of cut. At speeds on both sides of the minimum the actual depth sharply increases. Similarly, Figure 3 shows the data with reference to the width of the groove. The actual width is always significantly higher than the geometric width. This is due, of course, to the more or less well-developed "bird's wing type spalling" reported earlier which is basic to the stockremoval mode in brittle materials. Figure 4 shows representative profilometer traces, taken at one point across a workpiece with parallel grooves produced at various speeds. The same trend, as more precisely determined by measurements, with regard to depth and width, is indicated.

Total volume removed, as a result of increased depth and width of cut, therefore, significantly increases as wheelspeed is reduced or increased beyond a certain minimum. This minimum shifts to higher wheel speeds for higher modulus materials as shown earlier.[2] Increase in wheel speed beyond the minimum and generally beyond speeds that are presently

regarded as conventional grinding wheel speeds, results in sharply increased rates of removal with only minimal increases in grinding energy. This is not, of course, the case for a decrease in wheelspeed.

The above findings have considerable significance with regard to grinding wheel design and operating parameters. It is expected that grinding wheels of radically different design, in which particularly grain size, grain geometry and grain distribution are adjusted (or used) with reference to the appropriate operating parameters (particularly wheel speed), can significantly improve the efficiency of the stockremoval process on brittle materials. In any case, high wheel speeds will show: a reduction in grinding force and thus grinding energy, an increase in stockremoval rate, and as will be seen from Section IV a decrease in the rate of diamond wear, which further affects the force pattern.

II DESIGN OF PIEZOELECTRIC DYNAMOMETER

A. INTRODUCTION

Earlier experiments involving the measurements of force levels and force distribution during single point grinding operations have made use of a strain gauge type dynamometer. Such dynamometers have distinct limitations if information other than average force levels is required. Reference is made to high speed response needs for analysis at frequencies higher than those at which full response of the dynamometer is exceeded (see Section I) particularly if accurate quantitative data is required. There is furthermore a need for accurately recording the impulse (force versus time plot) of a single cutting event at speeds up to 10,000 feet/sec. If the nature of (brittle) fracture depends on system parameters or differs from material to material, for which there is ample empirical and physical evidence (see e.g. Section VI), it should be reflected in the single event impulse. Variability of type and nature of brittle fracture under otherwise identical conditions may, as our results have already indicated, be followed. A highly sensitive dynamometer is required for recording of meaningful diamond wear data (see Section IV). For these and other purposes a highly sensitive piezoelectric type dynamometer with response characteristics of stiffness and sensitivity specifically adapted to present research needs, has been designed and constructed and is described

below. It should be noted that recording of the exact input impulse is significantly impaired by the fact that the output, i.e. the recorded event, is a superposition of the dynamometer modulated input and the vibrational response of the dynamometer itself.

The design of the dynamometer was based on stiffness and sensitivity criteria of an elastic system subjected to a cyclic excitation. A dominant factor in setting stiffness criteria is the natural frequency of the dynamometer. The natural frequency of the dynamometer should be large compared to the maximum frequency of the exciting force or the actual cutting force exerted by the grinding wheel. By setting the ratio of the natural frequency to the maximum exciting frequency at about five (adopted as a design criterion), the natural frequency of the dynamometer lies well above the maximum frequency of operation and the influence of the vibration of the dynamometer on the actual cutting process is significantly reduced.

The next important factor is the sensitivity of the dynamometer. In general, the sensitivity of the dynamometer decreases as the rigidity increases. Since the dynamometer had to be designed for use under high speed grinding conditions (maximum speed $\sim$ 300 ft/sec) as well as low speed conditions ($\sim$ 30 ft/sec) it was essential to make the dynamometer stiff enough such that the natural frequency would always be well above the maximum operating frequency. This demands a relatively high degree

of stiffness resulting in a decrease in sensitivity. For this reason the strain gauge type sensor is generally not suitable for tracing the response characteristics of the dynamometer.

The resulting dynamometer with readout equipment is shown diagrammatically in Figure 5. Figure 6 shows an actual photograph of the instrument. A quartz force transducer has proven to be an ideal sensor for the purpose of the present experiment. Kistler (Model 912H) impact force transducers with the following specifications have been used: range 0 - 500 lb, resolution 0.002 lb, sensitivity 50 picocoulombs/lb, resonant frequency 60,000 Hz, rigidity $20x10^{-8}$in/lb, and rise time 10μ seconds. Since the transducer is capable of tracing the impact force which is acting normal to the surface of the transducer two transducers (see Figure 5) have been used to separately measure the tangential and normal response forces. The constraints resulting from the two trans-ducers are not enough to make the system dynamically stable and two major and eight minor constraints have been added.

The two transducers used for the present experiment have charge sensitivity of 48.5 and 50.2 pCb/lb, respectively. The charges generated by the transmitted impact forces are amplified by the charge amplifiers (Kistler Dual Mode Amplifier Model 504A) which convert the charge input directly into a force output in DC volts. The amplifier outputs are recorded by a Tektronic storagescope. By multiplying the conversion factor

HORIZONTAL TRANSDUCER

WORK PIECE

VERTICAL TRANSDUCER

CHARGE AMPLIFIERS

STORAGE SCOPE
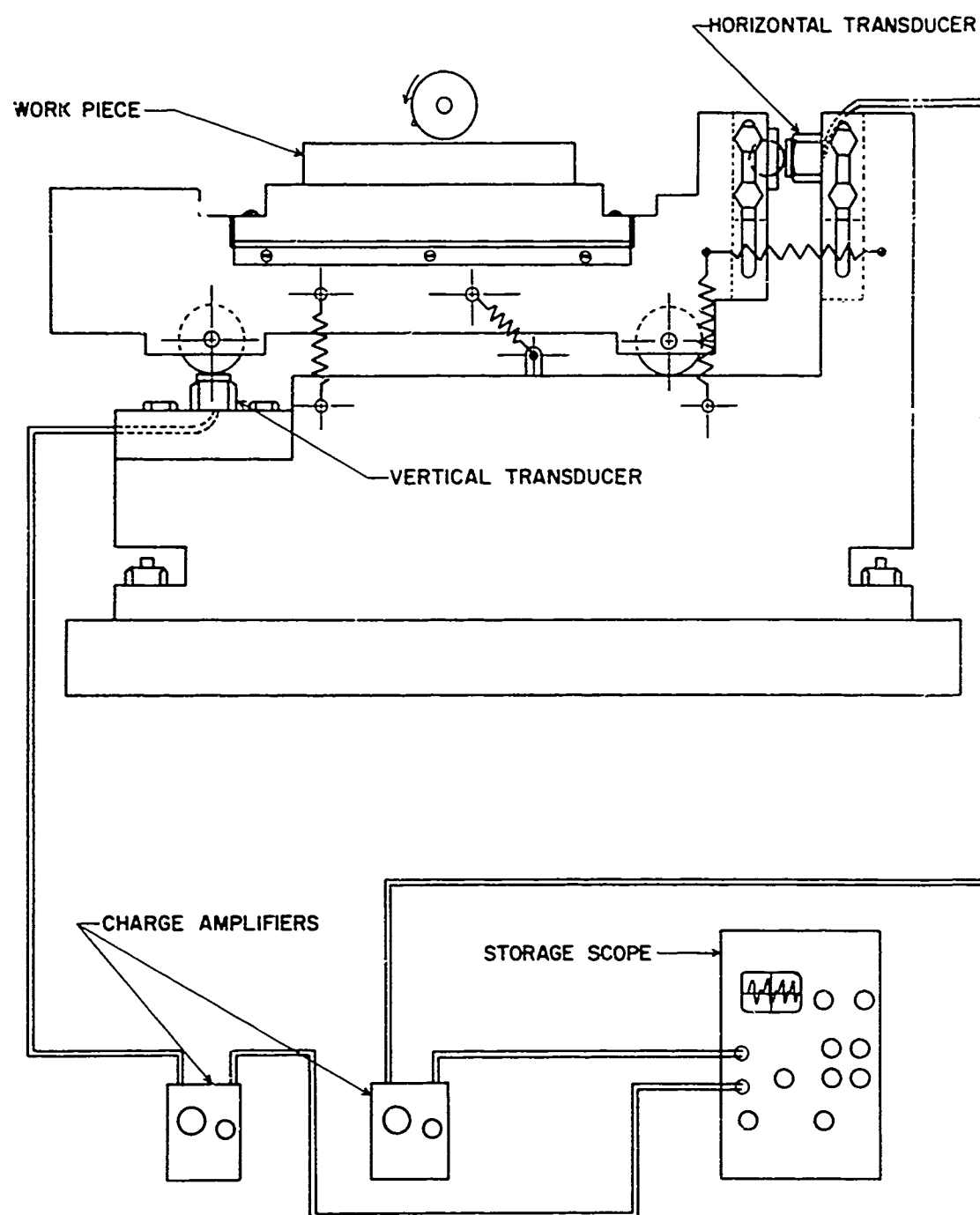
FIGURE 5. Piezoelectric Dynamometer (Schematic) with Readout Equipment.
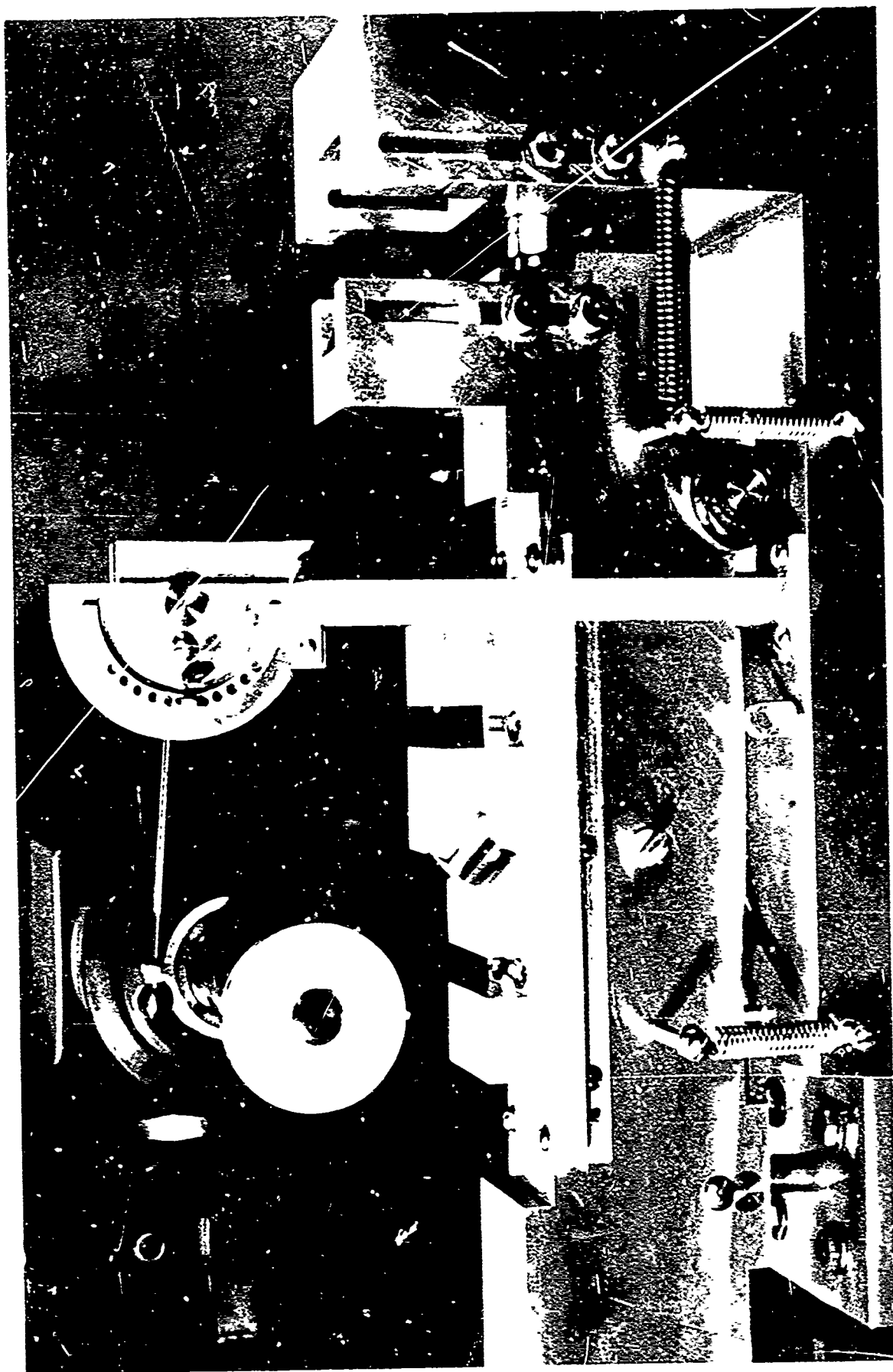
FIGURE 6. Piezoelectric Dynamometer with Calibration Stand in Place.

of the calibrated charge amplifier output with the scope output reading, one can easily obtain the response forces.

Further design criteria and features of the dynamometer are discussed in the following subsections.

B. MASS-SPRING-DAMPER MODEL ANALYSIS

Elastic structures have an infinite number of degrees of freedom since an elastic body consists of distributed mass and elasticity. They are accordingly capable of an infinite number of modes of vibration, each of which has a natural frequency the magnitude of which depends on the distribution of mass and elasticity. Vibration analysis of this type of system is generally so complicated as to be impractical. To simplify the vibration analysis of a dynamometer, which actually consists of distributed mass and elasticity with several constraints, it is replaced (see Figure 7) by an idealized model consisting of a massless spring, a springless mass and a damper.

The natural frequency of an elastic vibratory system is proportional to the stiffness of the body and inversely proportional to the mass of the system, $p = \sqrt{\frac{k}{m}}$. A light material with a high stiffness constant would therefore be an ideal choice. Since the stiffness of the system can be significantly increased by changing the geometry of the system (see equation 1) the dynamometer body was constructed from 7075-T6 aluminum
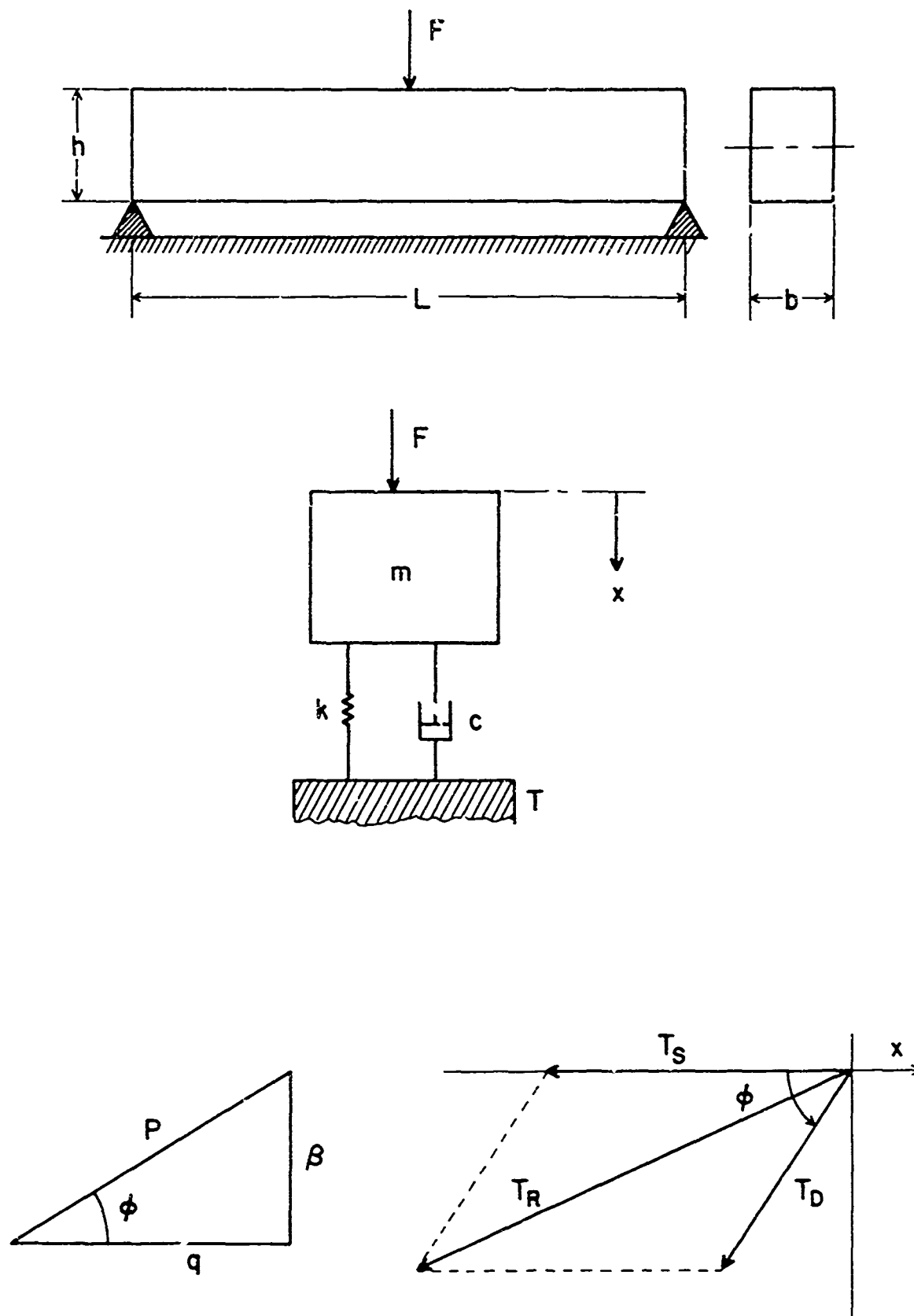
FIGURE 7. Idealized Model of Dynamometer
(see text for explanation)

(E = 10.4×10^6 psi, ρ = 5.42 lbf-sec^2/ft^4)* which is relatively light weight and has high stiffness. In Figure 7 the dynamometer, which is equivalent to a massless beam with uniformly distributed load, is replaced by a mass-spring-damper model. From the deflection analysis of an elastic beam the equivalent stiffness constant k can be expressed as

$$k = 76.8 \frac{EI}{L^3} \tag{1}$$

where

E = Elastic Modulus (psi)

L = length of dynamometer (in)

b = width of dynamometer (in)

h = height of dynamometer (in)

I = the second moment of cross section area

with respect to centroidal axis (bh^3/12 in^4)

k = equivalent stiffness constant (ib/in)

m = mass of dynamometer (1bf-sec^2/in)

The undamped natural circular frequency is,

$$p = \sqrt{\frac{k}{m}} \qquad \text{(rad/sec)}$$

$$= \sqrt{\frac{76.8 \ EI}{mL^3}} \tag{2}$$

_____

* E = Elastic Modulus and ρ = mass density.

and the natural frequency in cycles per second is,

$$f = \frac{1}{2\pi} \sqrt{\frac{76.8\ EI}{mL^3}} \tag{3}$$

The damped natural frequency for the underdamped condition, p_d, i.e., $c < c_c$ where c is damping coefficient and $c_c = \sqrt{km}$ critical damping coefficient, is

$$p_d = p(1 - \zeta^2)^{1/2} \tag{4}$$

where $\zeta = c/c_c$, fraction of critical damping.

The extent of the damping is indicated by a logarithmic decrement and is normally determined experimentally by either observing the transmissibility at the resonance of a system that is executing a forced vibration, or by noting the rate of decay of free vibration of the system. The contribution of damping to the natural frequency of the system, for the underdamped condition, is small ($\zeta = 3.183 \times 10^{-4}$) compared to unity and for design purposes an undamped analysis can be justified.

The operating range is 0 - 25,000 rpm resulting in a maximum frequency f_{max} = 417 cps. From the stiffness design criterion described above one can set

$$5\ f_{max} = \frac{1}{2\pi} \sqrt{\frac{76.8\ EI}{mL^3}}$$

$$= 8.0372 \times 10^4\ \left(\frac{h}{L^2}\right) \tag{5}$$

which establishes the limit of the height to length ratio of the dynamo-
meter. The final dimensions of the dynamometer based on ideal model
analysis was thus calculated from Equation 5. Similarly, the analysis for
the horizontal model of vibration was constructed. The final dimensions
of the dynamometer were subsequently arrived at with only minor changes in
dimensions and geometry within the allowable range established by the
design criteria. These changes were necessary for the following reasons:

1) to enable the use of previously used workpieces and
   holders of fixed dimension the values of h and L of
   the dynamometer were slightly adjusted.

2) to ensure that the centerline of the horizontal
   transducer coincides at all times with the line
   of action of the horizontal component of the
   cutting force, the body of the dynamometer is
   constructed in L shape maintaining the symmetry
   of the mass distribution with respect to the
   center of the workpiece.

3) the horizontal ball bearing in the main body of
   the dynamometer and the horizontal transducer are
   mounted on adjustable sliding blocks so that the
   center of the transducer can be aligned with the
   line of action of the horizontal force for different
   workpiece thickness.

4) to minimize the machine vibration, transmitted through the machine bed to the dynamometer, several stiff springs are attached between the main body of the dynamometer and supporting block. Use is also made of vibration absorbing pads between the supporting block and machine bed.

In order to calibrate the dynamometer under dynamic loading conditions, a special calibration apparatus, shown in Figure 8, was designed. The impact forces produced by the falling steel ball from different elevations are directly measured by locating the impact transducer at the point of impact. The transducer is mounted at 45 degrees to the horizontal surface of the dynamometer so that the measured impact force can easily be decomposed into normal and horizontal components. Next the transducer is replaced by a dummy transducer having the same surface conditions and dimensions as the real one, and the same test was repeated to obtain the response pulse at the horizontal and normal pick-ups attached between the main body of the dynamometer and its supports. The calibration transducer holder is designed such that the height is adjustable from .9375" to 1.625", which is the equivalent thickness range of the workpieces. Typical peak force calibration curves are given in Figures 9 and 10.

STEEL BALL D = 1/4 ~ 1/2"

TRANSDUCER
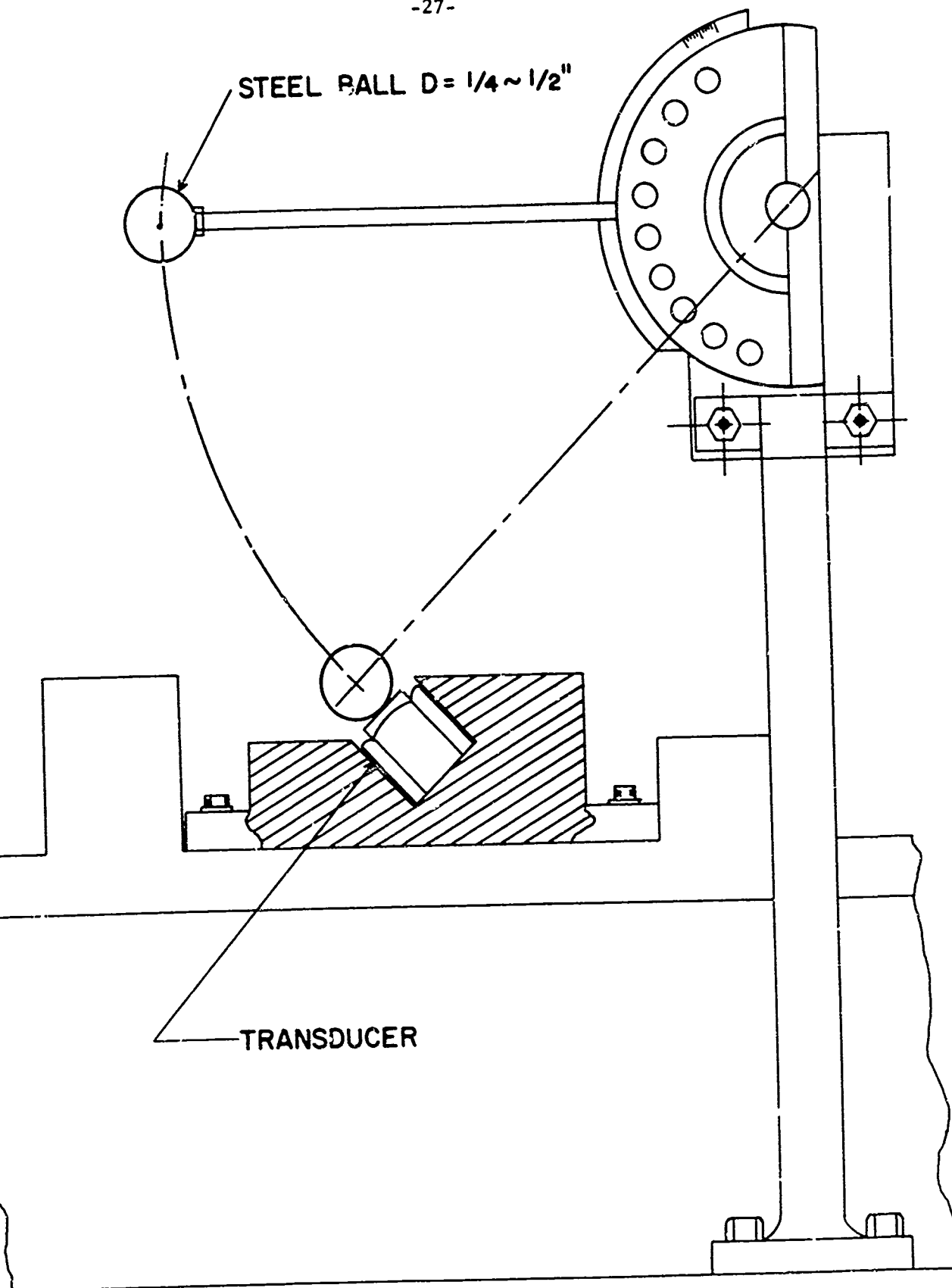
FIGURE 8.   Calibration Device for Horizontal and Vertical
Forces for Dynamometer of Figure 6.
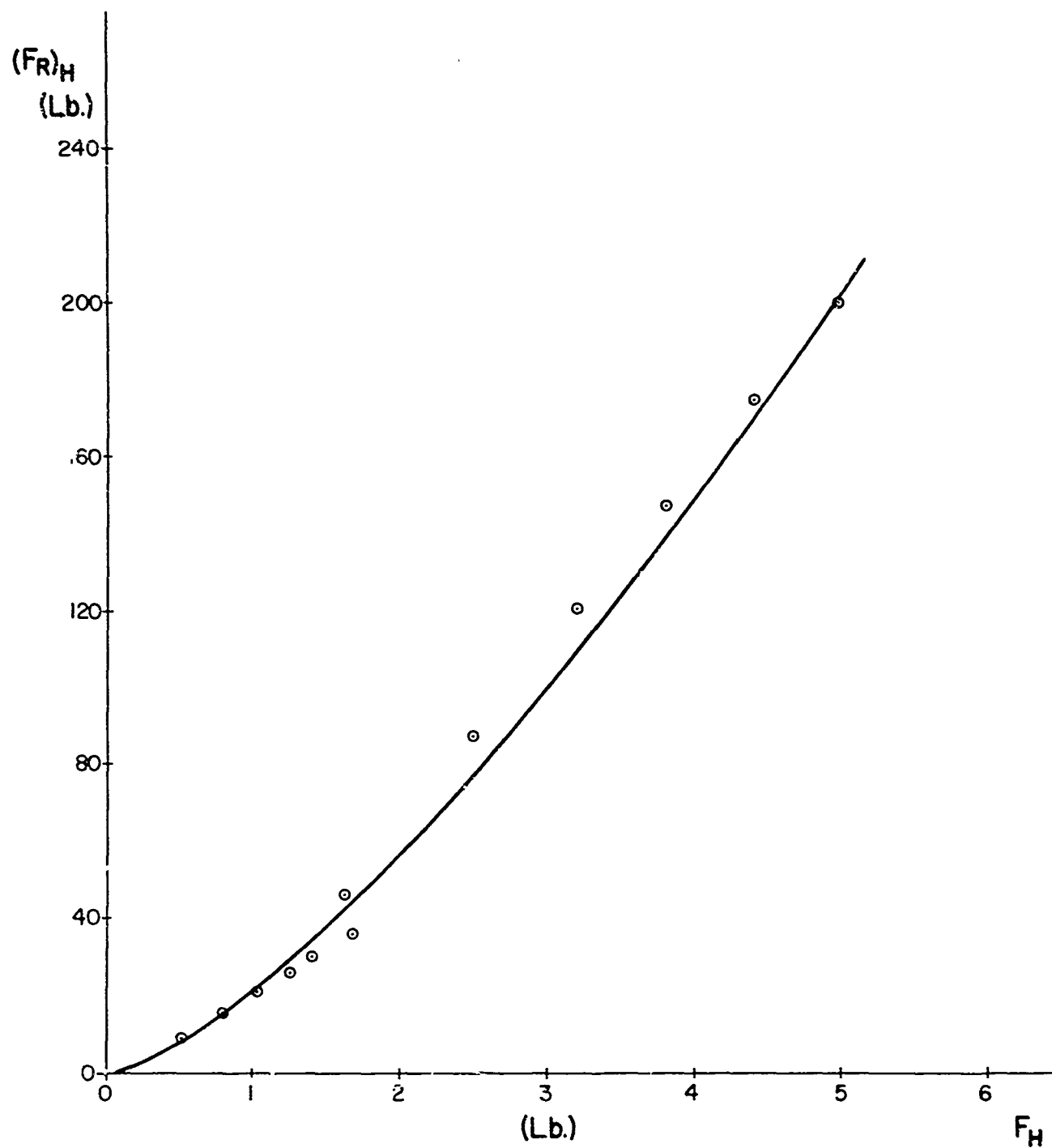
FIGURE 9. Calibration Curve for Horizontal Response Force, F_H, Versus Horizontal Real Force $(F_r)_H$.
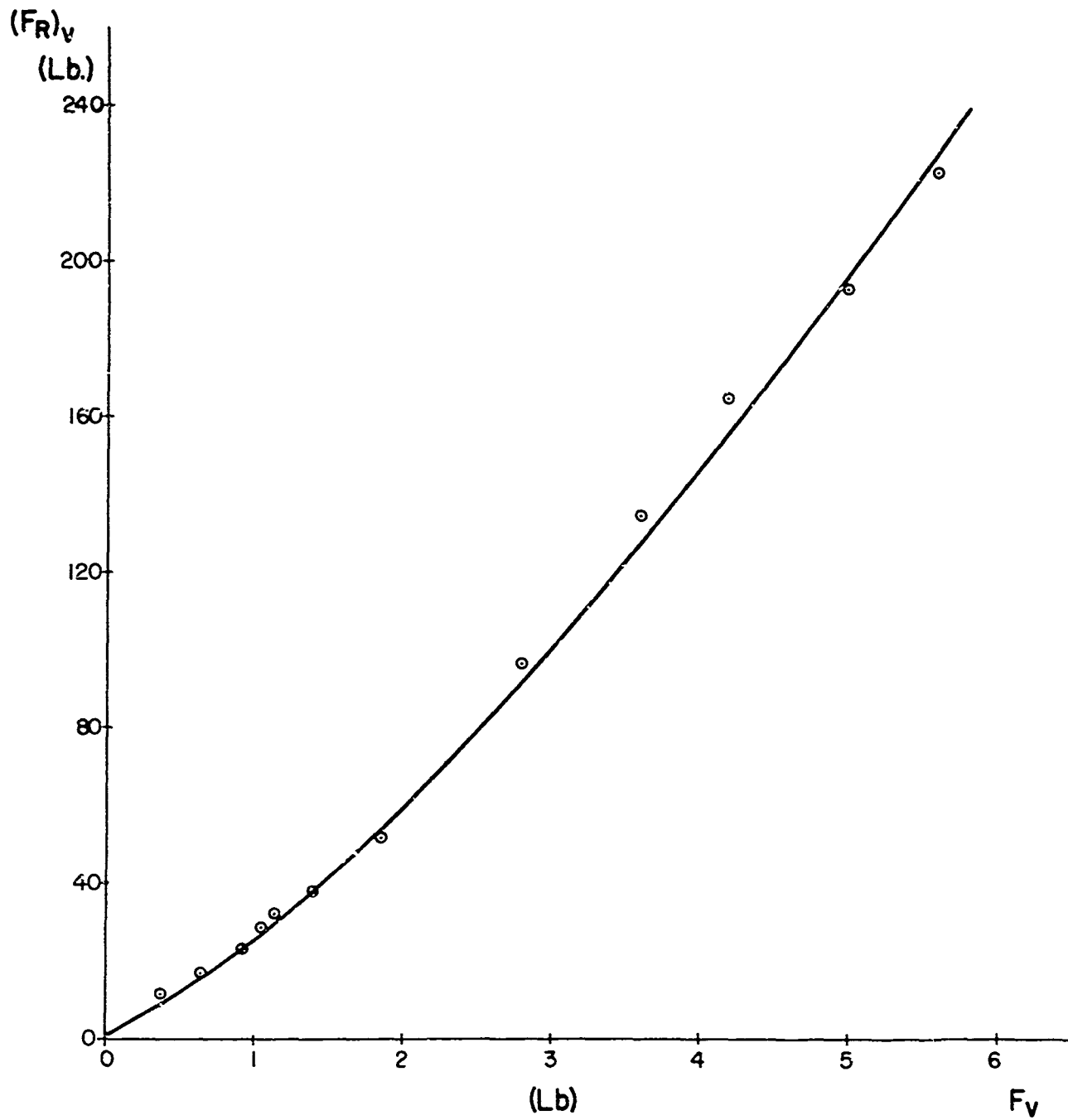
FIGURE 10. Calibration Curve for Vertical Response Force, F_v, Versus Vertical Real Force $(F_r)_v$.

C. IDEAL MODEL ANALYSIS

The governing equation of the motion of a mass-spring-damper system, shown in Figure 7, due to cyclic excitation of an external impulsive force with magnitude F and period τ is

$$\frac{d^2x}{dt^2} + 2q\frac{dx}{dt} + p^2x = \sum_{n=0}^{\infty} \frac{F}{m}\delta(t - n_\tau) \qquad (6)$$

where   x = displacement

q = c/m, damping coefficient/mass

p^2 = k/m, stiffness constant/mass

t = time

δ = Dirac's delta function

Using the Laplace transform defined as

$$\overline{x} = L\{x\} = \int_0^\infty xe^{-st}\,dt,$$

where s is transform parameter and the initial condition x (0) = 0 and $\dot{x}(0)$ = 0, the solution of equation (6) can be obtained as

$$x = \frac{F}{m\beta}\{e^{-qt}\sin(\beta t) + e^{-q(t-\tau)}\sin[\beta(t-2\tau)]\,u(t-\tau)$$

$$+ e^{-q(t-2\tau)}\sin[\beta(t-2\tau)]\,u(t-2\tau)$$

$$+ \ldots\ldots$$

$$+ e^{-q(t-n\tau)}\sin[\beta(t-n\tau)]\,u(t-n\tau)\,\} \qquad (7)$$

where

$$\beta = \sqrt{p^2 - q^2} \quad \text{and} \quad u(t-n\tau) \text{ is a unit step function.}$$

The response pulse due to a single blow of line impulse will be simply the first term in Equation 7. Similarly the response function due to a single blow of step and half sine wave types of input are obtained, respectively, as follows:

Step input response function = $F [u(t) - u(t-t_c)]$

$$x = \frac{F}{mp^2} \{ 1 - e^{-qt} \cos \beta t - \frac{q}{\beta} e^{-qt} \sin \beta t$$

$$+ [-1 + e^{-qt} \cos \beta (t-t_c) + \frac{q}{\beta} e^{-qt} \sin \beta (t-t_c)] u(t-t_c) \} \qquad (8)$$

Sine wave input response function,

$$= F_1 \sin (\frac{\Pi t}{t_c}) [u(t) - u(t-t_c)]$$

$$x = \frac{F_1 \Pi}{mt_c} \{ A e^{-qt} \cos \beta t + \frac{B-Aq}{\beta} e^{-qt} \sin \beta t$$

$$+ C \cos (\frac{\cdot}{t_c} + \frac{Dt_c}{\Pi} \sin (\frac{\Pi t}{t_c}) \}$$

$$+ \frac{F_1 \Pi}{mt_c} \{ A e^{-q(t-t_c)} \cos \beta (t-t_c) +$$

$$\frac{B-Aq}{\beta} e^{-q(t-t_c)} \sin \beta (t-t_c) + C \cos [\frac{\Pi}{t_c} (t-t_c)]$$

$$+ \frac{Dt_c}{\Pi} \sin [\frac{\Pi}{t_c} (t-t_c)] u(t-t_c) \qquad (9)$$

where

t_c = cutting time

F_1 = maximum of input sine wave

$$A = \frac{2q}{(\gamma^2 - p^2)^2 + 4q^2\gamma^2}$$

$$B = \frac{\gamma^2 - p^2 + 4q^2}{(\gamma^2 - p^2) + 4q^2\gamma^2}$$

$$C = \frac{-2q}{(\gamma^2 - p^2)^2 + 4q^2\gamma^2}$$

$$D = \frac{p^2 - \gamma^2}{(\gamma^2 - p^2)^2 + 4q^2\gamma^2}$$

$$\gamma = \pi/t_c$$

The force experienced by the support is the sum of forces transmitted by the elastic element k and damper c. These two forces are not generally in phase, i.e., they do not reach their maxima simultaneously and must, therefore, be added vectorially.

In order to demonstrate a method for calculating the transmitted force, a simple response function resulting from a single line input is derived. In this case the forces transmitted by the equivalent spring with spring constant k and the damper c, are, respectively

$$T_s = \frac{F_1 p^2}{\beta} e^{-qt} \sin \beta t \tag{10}$$

and

$$T_d = - \frac{2qpF_1}{\beta} e^{-qt} \sin (\beta t - \phi)$$

where the phase angle

$$\phi = \tan^{-1} \frac{\beta}{q} \tag{11}$$

The resultant of the transmitted forces then becomes

$$T_r^2 = T_s^2 + T_d^2 - 2 T_s T_d \cos (\Pi - \phi)$$

$$\left(\frac{T_r}{F_1} \right)^2 = \frac{p^2}{p^2 - q^2} e^{-2qt} \{ p^2 \sin^2 \beta t + 4q^2 \sin^2 (\beta t - \phi)$$

$$- 4pq \sin (\beta t) \sin (\beta t - \phi) \sin \phi \} \tag{12}$$

Extending this analysis in a similar fashion to the cyclic loading case, one can establish a force response function in terms of the vibration parameters of the dynamometer. Once the response force and input force are determined by the calibration method described in (II B) a system of simultaneous algebraic equations for unknown parameters can be obtained. If the parameters, expressed implicitly in the system of equations, are determined by means of a digital computer an equation relating input and response forces for the dynamometer will be determined. Such an analysis is presently in progress.

D. PRELIMINARY ANALYSIS OF RESPONSE PULSE

Typical response traces of the dynamometer are shown in Figure 11 and Figure 12. The shape of the response pulse reflects mainly the dynami: characteristics of the dynamometer which is excited by an impulsive force with very short time duration compared to the natural period of the dynamometer. From the macroscopic mechanics point of view, the average impulse force generated by each cut is reflected on the response trace by the maximum peak of each cutting event. On an expanded time scale trace, Figures 11-12 Top show the response pulses and one full cycle of cutting, i.e. one full wheel revolution, in which a sharp maximum peak represents the actual cutting event. Figures 11-12 Bottom show the long time scale output for one complete 4" long cut on AD 85 ceramic. This type of output is very important for the average input energy analysis which is one of the objectives of the present experiments. The nonuniformity of the peak force output value is due to the inhomogeneity of the finished workpiece surface of the ceramic and horizontal nonparallelism of the cutting surface. Extreme care was taken to achieve horizontal parallelism during each cut since it is a factor which could contribute a large error in computing the average impulse force. For instance, an error of .0005" depth of cut could generate five to twenty percent of error in the output force depending upon the material being cut and the depth of cut initially set. Another factor which plays a role in the nonuniformity of the value

FIGURE 11. Tangential Response Pulse Characteristics on AD 35
(6000 rpm, .002" Depth of Cut, amp. range = 100).
Top: Vertical Scale, .02 v/div, Horizontal Scale
1 msec/div. Center: Vertical, .05 v/div.,
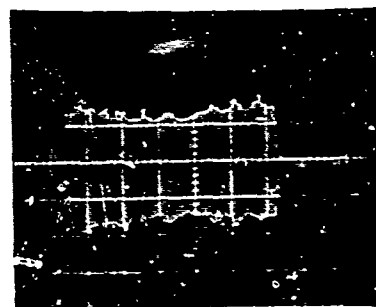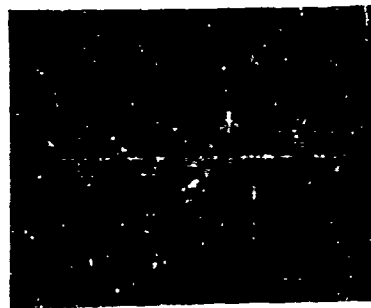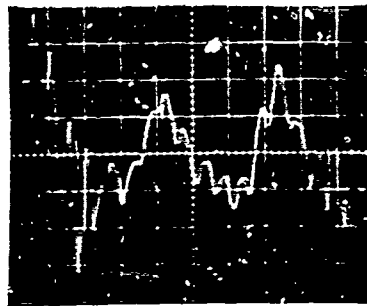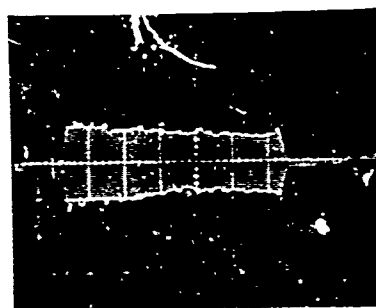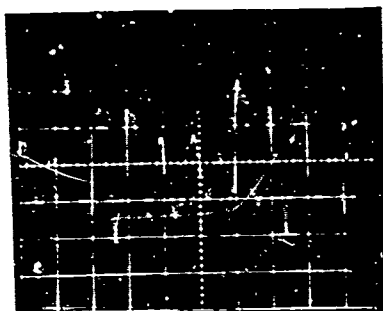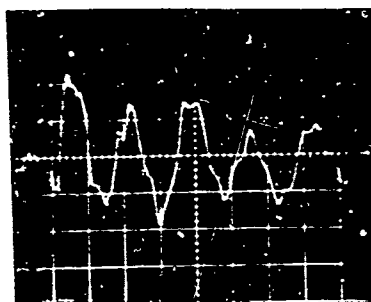Horizontal 2 msec/div. Bottom: Vertical .05 v/div.,
Horizontal .5 sec/div.

FIGURE 12. Vertical Response Pulse Characteristics on AD 85
(6000 rpm, .003" Depth of Cut, Amp. Range = 100).
Top: Vertical Scale, .05 v/div., Horizontal Scale
1 msec/div. Bottom: Vertical .02 v/div.,
Horizontal .5 sec/div.

of the peak force output is the change of wheelspeed during the cutting event. As the depth of cut increases from .001" to .003" the pattern of the "squeezed" output becomes either concave or shows an exponential type of decay, especially in the low wheel speed ranges. This phenomenon becomes less apparent as wheelspeed increases and depth of cut decreases. This clearly indicates that when greater cutting forces are experienced, the wheelspeed tends to decrease during the initial period of cutting.

The number of waves between each cutting event, shown in Figures 11 and 12 is a function of the exciting frequency and the natural frequency in the normal or tangential direction of the dynamometer. The number increases as the wheelspeed decreases. For instance, the number of the damping waves shown in Figures 12T and 12C is the normal output during one full period of cutting is six at 6,000 rpm. If the exciting frequency is doubled the number should be three, which is the exact result obtained from the response wave at 12,000 rpm. The small waves that appear on the large waves are mainly due to the characteristics of the dynamometer. The number of small waves is, in general, the ratio of cutting period to the natural frequency of the dynamometer in the normal or tangential direction. Therefore, as the exciting frequency increases this number should lineraly decrease for a fixed depth of cut. The result shows that the pattern of increment is not linear. This can be interpreted to mean that the input pulse, which might have different characteristics for different materials at different wheelspeeds, is superimposed on the

distorted waves due to the dynamometer characteristics. The determination of the exact force distribution pattern during the actual cutting is presently under study. A correlation between the input force distribution and microscopic aspects of the nature of material fracture can ultimately result.

III CERAMIC STOCK REMOVAL PHENOMENA

A. GENERAL

In order to supplement the after-the-fact evidence of the stock removal phenomena, such as available through (SEM) examination of the workpiece and diamond, and assist interpretation of force records, further elucidation of the in situ stock removal events has been sought through high speed photography. It is further anticipated that crack patterns may be followed during the grinding of transparent ceramics. Whereas such experiments seemed readily accessible in principle, the recording of the actual desired event meets with considerable difficulty. The use of a two and one-half inch diameter wheel as opposed to the previously used seven inch configuration has, with all the advantages for other aspects of our investigations, proven to increase the problems. The actual field of view of interest is for all practical purposes confined to an area 3/4 x 3/4 of an inch in such a way that the top of the workpiece and the diamond tip are included with sufficient area available to record the flying debris. Under these conditions the arc of travel for the diamond is ~14°. If the depth of cut is chosen at 0.003", the total contact of the tool with the workpiece is limited to 7° of arc. Two basically different approaches have been used: continuous light high speed photography and synchronized flash photography. A variant on the former, streak photography, has been tested for feasibility.

B. CONTINUOUS LIGHT HIGH SPEED PHOTOGRAPHY

A standard high speed camera* was used to record the stock removal events on 16mm film. Standard lenses on this type of camera are wide angle type lenses (82° in our case) which are unsatisfactory because of their low magnification and very low resolution. The lens system was therefore replaced with 55mm Nikor lenses, f1.4 and f3.5 respectively, including extension through tubes or bellows to effect the desired magnification. It was later found that the internal prisms and reflecting mirrors in the camera limit the optical system to f3.5 so that there was no point in using particularly fast lenses. The f3.5 lens was therefore used. It provides better possibilities for magnification and better depth of field. It has been possible to get 1/1 to 4/1 magnification with the lens located 4 to 8 inches from the subject in this way.

The most important factor in determining the quality of the high speed photography is the available light, which also sets limitations. The intensity of the available light was measured with a 1/20° Honeywell Pentax lightmeter. The total field of view was 20° and the spot reading was limited to 1°. It is ideal for the application. For continuous light application 3 quartz-iodine lamps, 650 watts each, were used with infrared filters. They were located only 10-15" from the field of interest.

---

*
Hycam, 8000 fps, 100 ft. spool film 16mm, interchangeable shutters from 1/2.5 to 1/200.

This provided maximum available light for the specific application. The presence of addi ional (2 x 1000 watts and 2 x 650 watts) reflected lights located 3 to 4 fert from the subject did not improve the intensity of light. A maximum reading of 19 eV on a 24 eV scale for the light intensity was the limiting condition for the application. For reasons of internal optics limitations and decrease in available light as a result of magnification, a five stop decrease from the actual light reading had to be tolerated. Under these conditions and at a light level optimized by focusing with the help of Fresnel lenses resulting in a 20 eV maximum reading, the camera could not be run fast enough to produce acceptable pictures. Blur calculations show that at a wheel velocity of 5000 rpm and a camera speed of 2000 fps (light level 18 eV) the wheel travelled ~0.13" during the time the shutter was open. An increase in light level to 20 eV affords an increase of the film speed to 4000 fps which still indicates excessive travel of the wheel during the exposure time. It was finally attempted to solve the light problem, or obtain higher frame speeds, by going from the 400 ASA reversal film normally used to a 1250 ASA experimental black and white negative film requiring special processing procedures not available in our laboratories. The high speed film allowed frame speeds of 8000 fps under maximum light conditions. Wheel travel during exposure time has now been reduced to 0.003".

The results under these optimal conditions are shown by way of example in Figures 13-14. In the running movie, travel path, strike pattern, chip removal, chip size and chip flow pattern may be observed but not with the needed clarity. Satisfactory blur-free high speed photography should be done under conditions producing not more than 0.001" of subject travel during exposure time. This would mean a minimal improvement by a factor of three over our optimal conditions. A camera would have to run at 24,000 fps plus. Such equipment is available at 1/2 and 1/4 frame exposures on 16mm film. This would put severe limitations on resolution after needed magnification, particularly with the very coarse grained high speed film already used, provided light conditions can be matched to these conditions. It is unlikely that high speed macrophotography at sufficient magnification ratios can be used for routine recording of the stock removal event. For these reasons we have shifted our efforts to the techniques described in Section IIIC.

Streak photography has been applied successfully. Our high speed camera could be conveniently modified by replacing the eye piece with a 50mm f1.4 lens for continuous recording and inserting a streak slit system. Clear records are obtained. At this time only feasibility studies were made and no further exploitation was undertaken. It will be possible to determine slow down of the wheel during cutting, an effect which appears real under certain conditions, and chip velocity as well.
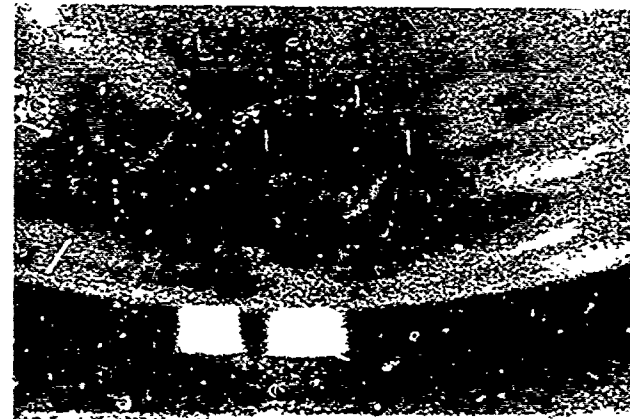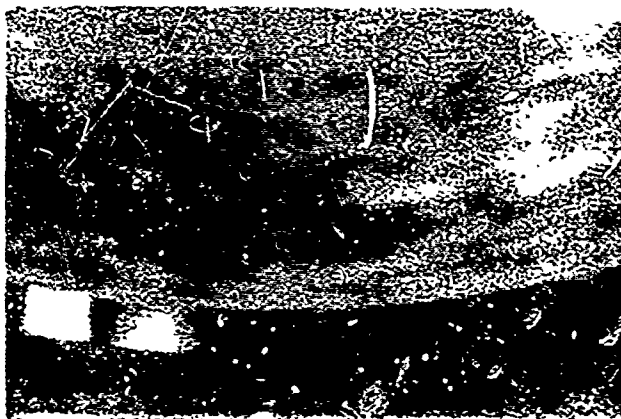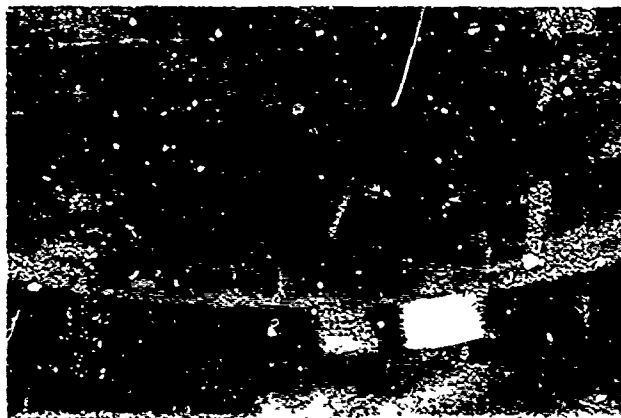
FIGURE 13. Single Frame Sequence from .iigh Speed Movie Film
of Cutting Event on AD 85 ⟨Wheelspeed 6000 rpm,
Depth of Cut 0.003", C૮ ₋erε 5000 fps). Time Between
Frames 8×10^{-2} msec. Order of Events, Left to Right -
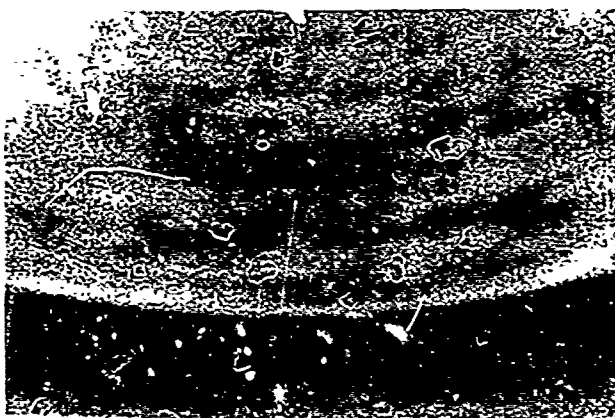Top to Bottom. Magnification 5X.

FIGURE 14. Continuation of Figure 13. Order of Events,
Left to Right - Top to Bottom.

High speed photographic records have verified our findings that stock removal takes two forms: removal in front of the diamond or in the path of the diamond trajectory resulting in extremely fine dust-like particles traveling at high speeds and removal from the side of the groove resulting in much larger spall particles traveling at much slower speeds.

C. SINGLE FLASH HIGH SPEED PHOTOGRAPHY

In order to eliminate the disadvantages of insufficient light intensity and film speed, recourse was taken to microsecond exposure techniques through so-called stroboscopic illumination. Synchronization of the cutting event and picture taking is accomplished through a photoelectronic pick-off device which is sensitive to reflections from tape on the wheel in combinations with a delay unit. In such a way the actual cutting event can practically be "dialed in" and a picture taken. The film is stationary and there are no limitations on film movement. Since there is no film movement, successive event recording, if it is desired for the same cut, will have to be obtained through multiple exposure. This requires the availability of several flash units with the ability to activate them successively during the cutting cycle which is normally counted in microseconds. If events from single cut to single cut could be regarded repeatable, one could synchronize with the start of one cut and take the next photograph of another cutting event slightly ahead of start, etc. In such a way, a complete running account may be built up.

Difficulties are those already mentioned under high speed photography. Light intensity requirements are severe at high manifi-cation. Use of 3000 ASA (polaroid) film at a magnification of 2x or 3x using a fast lens and two stroboscope units does give very clear photographs. An example is shown in Figure 15. Efforts are presently made to obtain an essentially continuous record.

FIGURE 15. Example of the Capture of Cutting Event Through Single Flash High Speed Photography and Photocell Synchronization. Wheelspeed 6000 rpm, Depth of Cut 0.003", Flash Speed 0.8 microseconds. Magnification 14.5X. Note Blurr-Free Detail. Capture of Chips Needs Improvement.

IV DIAMOND WEAR STUDIES

A. FORCE ANALYSIS

Knowledge of the extent and type of diamond wear in the ceramic
grinding process, particularly as a function of grinding parameters, is
of obvious significance particularly with regard to the economic aspects
of the process. Diamond wear is normally measured as a bulk effect by
following the decrease in diameter of a grinding wheel during normal
grinding leading to the well-known expression for systems performance:
the grinding ratio. Such measurements do serve an obvious purpose but
do not answer questions with regard to why and how diamond wears under high
velocity impact on ceramics. Furthermore, reduction in size is not the
only way in which a wheel diameter change may be registered nor does it
reflect actual performance in terms of material removed. Changes in
geometry rather than volume reduction has, as we have shown before, a
significant influence on performance. In addition, "wear" should be
analyzed along with force data, volume removed and its effect on the as-
finished product. Initially the problem lies in generating quantitatively
significant data. What is to be used as a measure of wear? When is a
diamond "worn"? The experiments and results reported on below have initiated
our attempts to put wear on a quantitative and comparative basis and to
have available a method whereby wear can be evaluated under a variety of
conditions particularly environmental change.

The availability of our new high sensitivity piezoelectric dynamometer and the ability of examining individual impact events forms the basis of our wear studies. Using a diamond point with which almost one hundred cuts (one cut = 4 inches of the length of the workpiece) were made on one type of material and under identical conditions it was noticed that the force level had increased almost twofold. A visual inspection of the diamond did not show any significant wear. When a new diamond point was used and the test repeated, the force values dropped to those generated in the initial test. Subsequent examination of the point after testing with the aid of scanning electron microscopy did reveal wear which is discussed in the following subsection.

In order to gain an understanding of the rate of wear and the possible influence of the workpiece material, tests were run on three different workpieces (AD 85, AL 500 and AD 99.5) under identical conditions, using new points for each material and following the force behavior as the tests went on. All tests were run at 6000 and 12,000 rpm and 0.002" depth of cut except for AD 85 which were run at 0.003" depth of cut. The results are shown in Figures 16 and 17. Data is presented in terms of total length of cut, i.e. number of cuts times the length of the workpiece and ΔF_H, the percentage increase of the horizontal component. The horizontal force value during the initial cut formed the basis of computing the percentage force increase. Depth of cut was checked and/or reset for each individual cut and workpieces were carefully levelled to insure that any

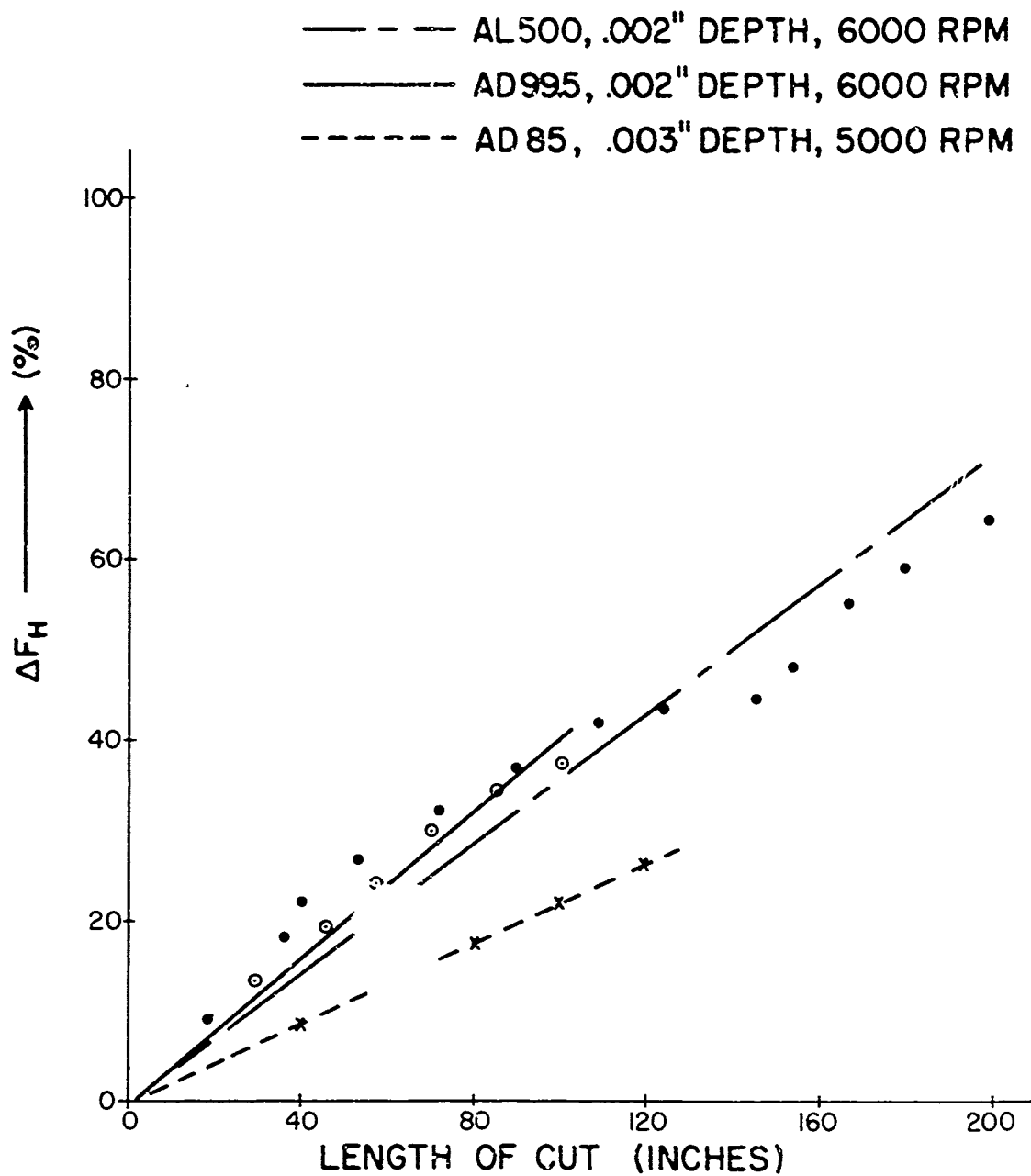FIGURE 16. Diamond Point Wear Measured by Horizontal Cutting
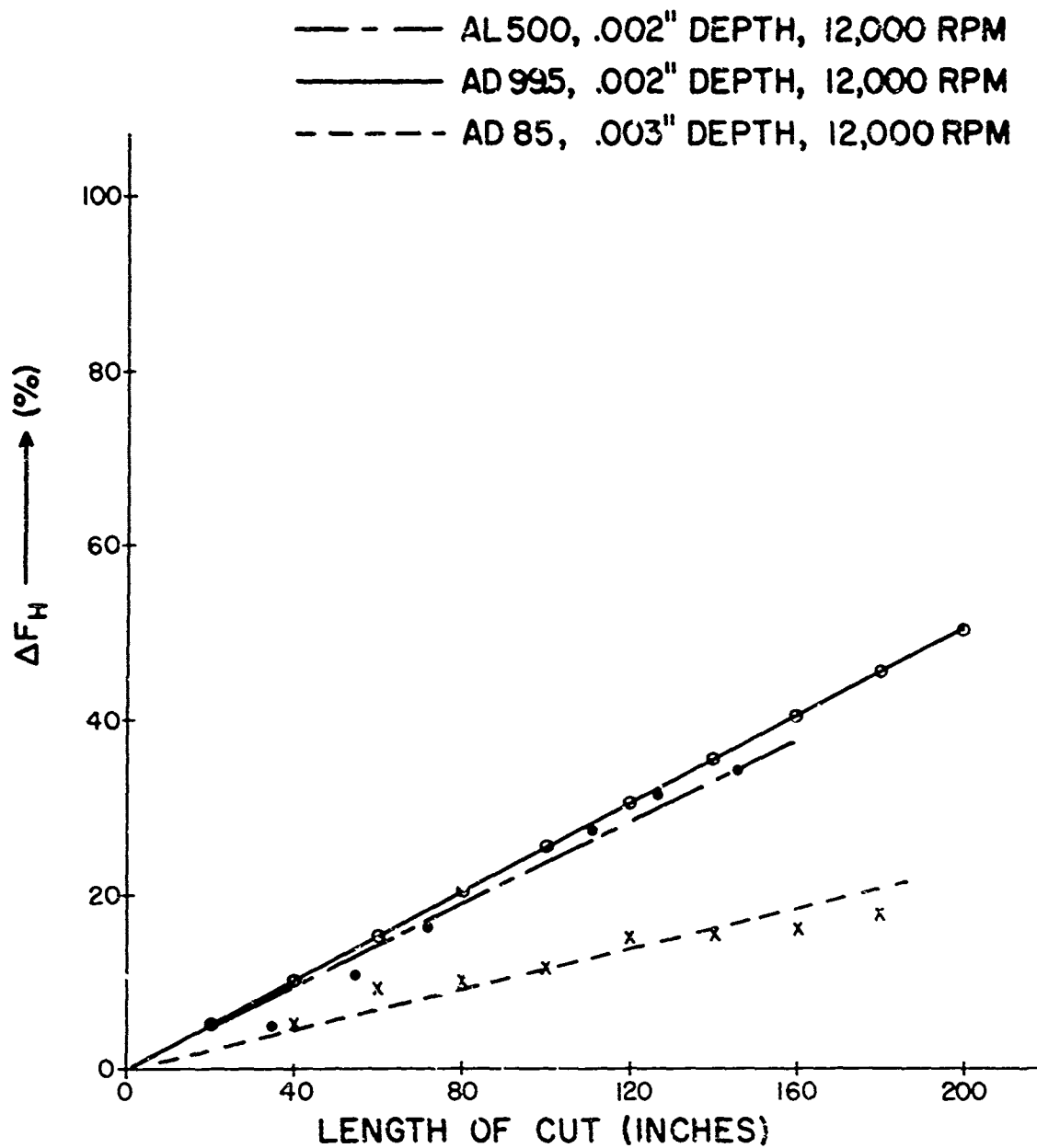Force at 6000 rpm. ΔF_H Versus Total Length of Groove Cut.

FIGURE 17. Diamond Point Wear Measured by Horizontal Cutting
Force at 12,000 rpm. ΔF_H Versus Total Length of Groove Cut.

increase in force level would be attributable only to point wear. The results indicate remarkable linearity of an increasing force as more and more material is ground in all three cases. Wear is consistently higher at the lower wheelspeeds which must reflect the higher forces needed at these speeds as indicated earlier[2] and again verified by data presented in this report (Sections I and V). Wear rates are also dependent on the material type with rate of wear increasing from AD 85 to AL 500 and AD 99.5 Although it would be premature at this point to indicate the primary material parameter(s) leading to wear, it is of interest that hardness (Rockwell 45N), percent alumina content and, as a result, density have the following increasing values for AD 85, AL 500 and AD 99.5 respectively: Hardness 75-78 and 81, percent alumina 85-94 and 99.5 and density (g/cc) 3.42-3.67 and 3.84. The significance of crack length and crack density (distribution), see Section V, in generating the force levels may have a bearing on the wear phenomenon. Wear rate is therefore proportional to the forces generated during cutting and the material parameters. So far all experiments were done dry (ambient conditions no grinding fluids supp.ied). Experiments are underway to detemine the effects of environment changes and the wear behavior as length of cut is drastically increased. See the following section on the nature of wear (not the extent) and its influence on force increase.

B. SCANNING ELECTRON MICROSCOPY

New and "worn" diamond points have been examined with scanning electron microscopy. Some of the initial results are given here by way of illustration of the nature and extent of the effect only. It is intended to have full correlation of the force data and SEM evaluation as the work progresses.

Figure 18 shows a new diamond point, as received, before any cutting has been done. The usual inhomogeneities, even with fine grinding and polishing, are apparent. The edges are, however, very straight with a near perfect radial tip. Blotches are probably due to lack of sufficient cleaning of the points before (metal) evaporation in preparation for SEM work.

Figure 19 shows two views of a point after 36 passes at 0.002" depth of cut, 6000 rpm on AD 99.5. The build up is believed to be heavily worked ceramic material. Direction of cut was not marked on these specimens but the crater (bottom picture right of center of Figure 19) probably developed at the leading edge. Subsequent observations of points on which the direction was noted have verified the predominant wear to take place at this point. The need for very careful high power SEM type observation is indicated by the fact that even at 50X virtually no wear detail is observable.

-54-
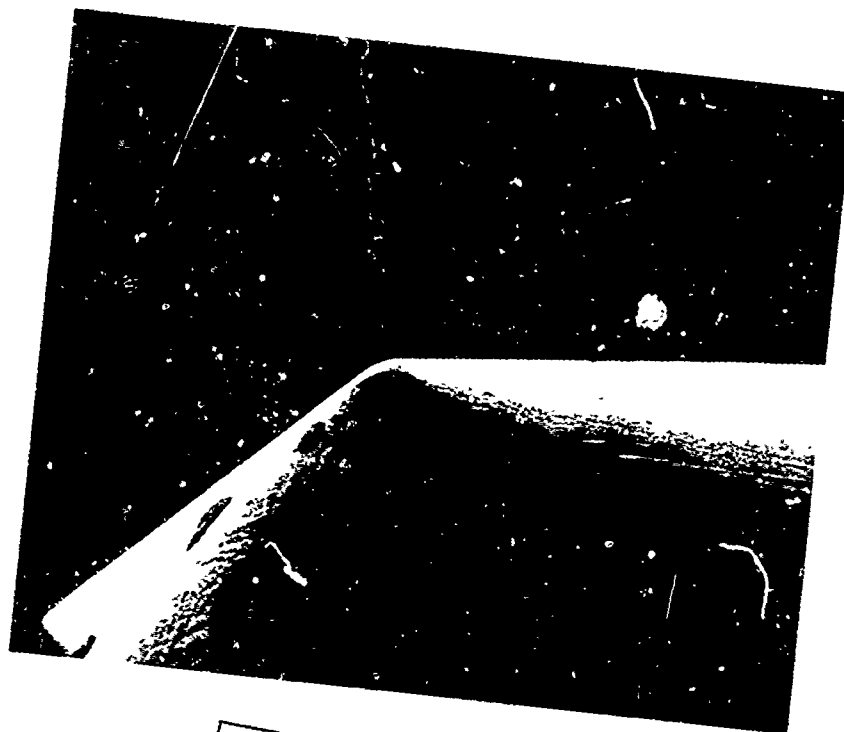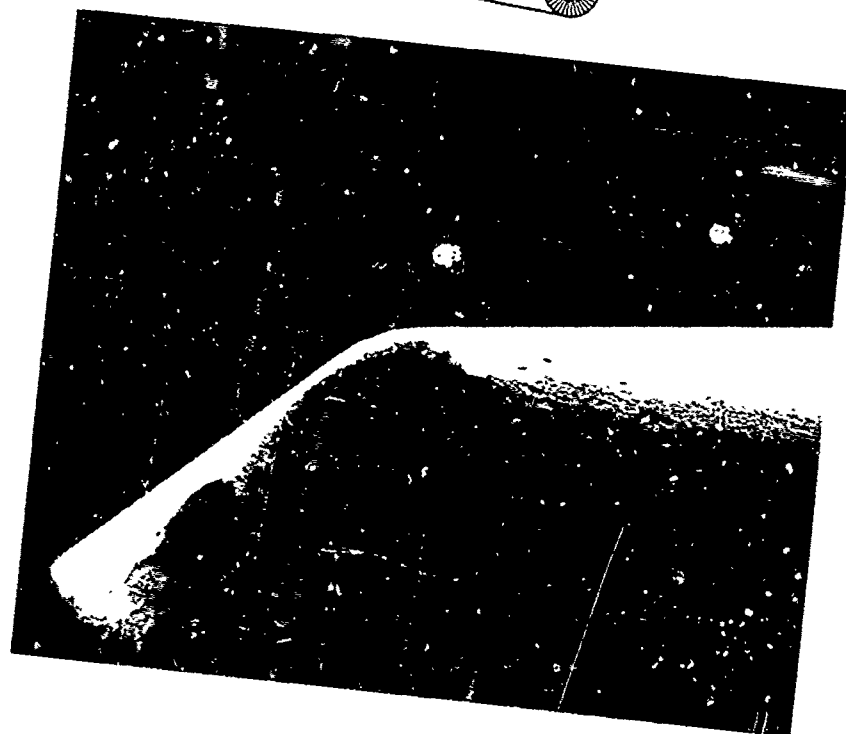
FIGURE 18. Scanning Electron Micrograph of New Diamond Point.
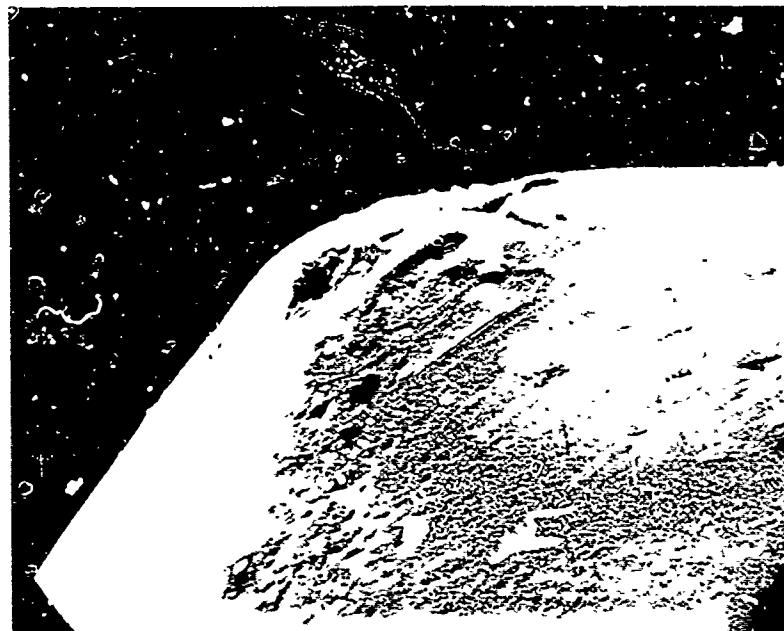Top 200X, Bottom 500X.
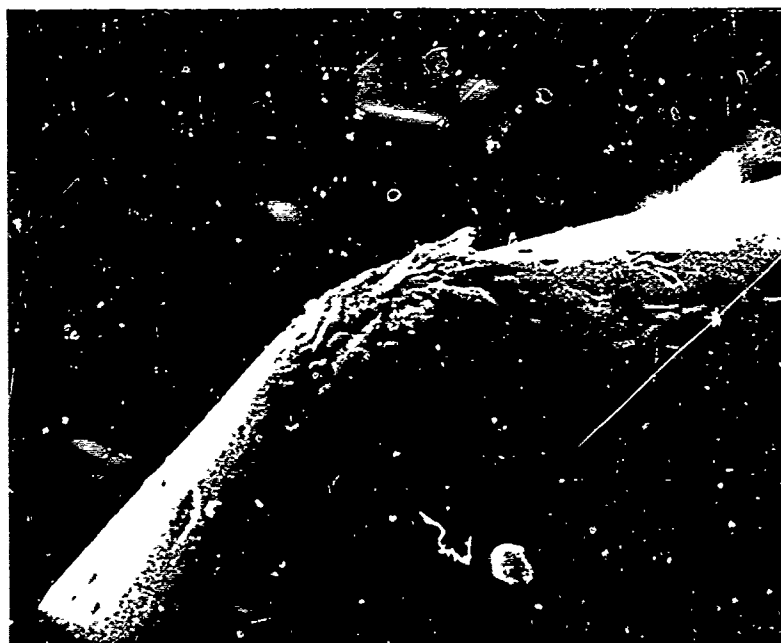
FIGURE 19.   Scanning Electron Micrograph of Diamond Point After
36 Passes, 0.002" Depth of Cut, 6000 rpm, on AD 99.5.
Top 500X Side View.   Bottom 500X Top View.
Explanation See Text.   Each Pass = 4 Inches.

Figure 20 shows top and side view of a point which had made
20 passes on five different aluminas and a variety of grinding conditions.
Note the essential preservation of a radius on the tip (not necessarily
the original radius) but much "pluck out" or "cratering" type damage
below and (probably) on the leading edge. Apparent absence of adhering
ceramic may be due to it not being present in this sequence or its ultimate
removal during final cycle or subsequent cleaning.

Figure 21 shows a point which has seen the most extensive cutting
in this series, namely 80 passes (approximately 320 linear inches of
actual cutting) on a variety of materials and under varying conditions.
It does show the most extensive damage in terms of depth and extent along
the diamond edge. The four pointed star effect may be related to the four-
fold crystallographic direction of the diamond although we have no evidence
to this effect. Figure 22 shows the same point in top view. A very
gradual wear resulting in the development of a flat on the tip is indicated.
There is a finite possibility of this flat being a crater filled with
ceramic although it is held unlikely because of the circular nature of the
periphery of the flat. The development of these flats may not be
noticeable until appreciable cutting has taken place. The point in this
example has seen the most wear of any point shown in this series.

Figure 23 shows top and side views of a diamond which made 45
passes (at 0.002") in AD 99.5, but at 12,000 rpm rather than the more
traditional 6000 rpm for all cases discussed above. There is very little

FIGURE 20. Scanning Flectron Micrograph of Diamond Point After
20 Cuts on a Variety of Aluminas (0.002" Depth of Cut.
6000 rpm). Top 500X Side View. Bottom 500X Top View
Each Pass Approximately 4 inches.
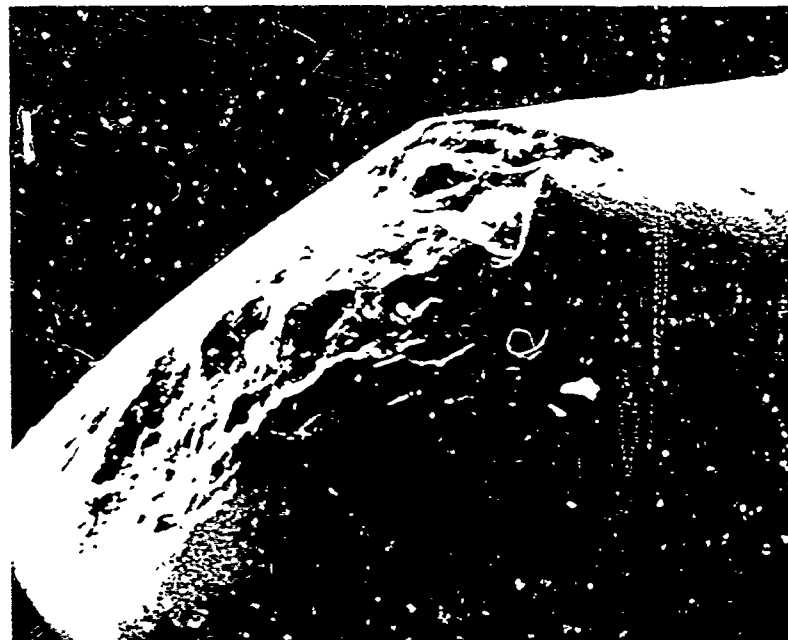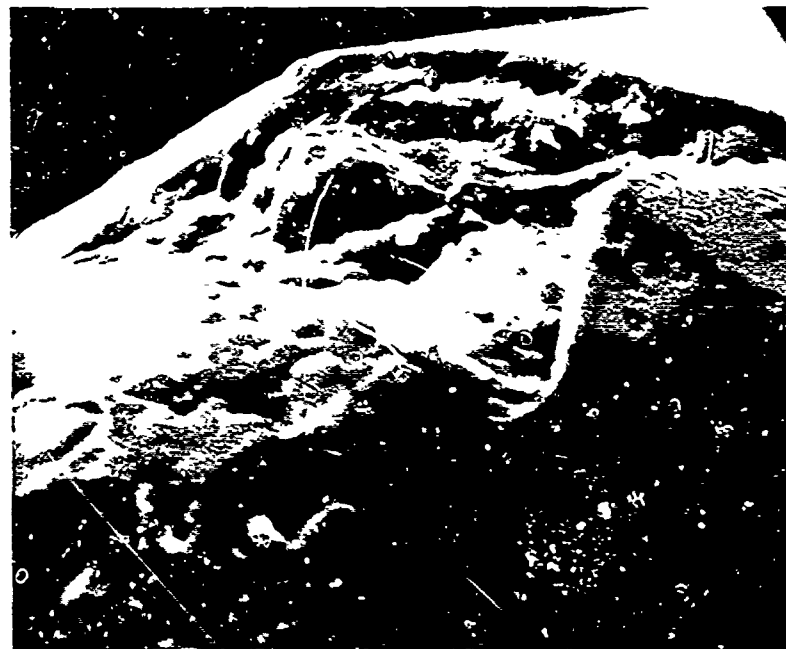
FIGURE 21. Scanning Electron Micrograph of Diamond Point After
320 Linear inches of Cutting on a Variet of Materials
and Under Varying Conditions. Top 200X, Bottom 500X.

FIGURE 22. Scanning Electron Micrograph of Point Shown
in Figure 21, 200X Top View. Note Development
of Flat.
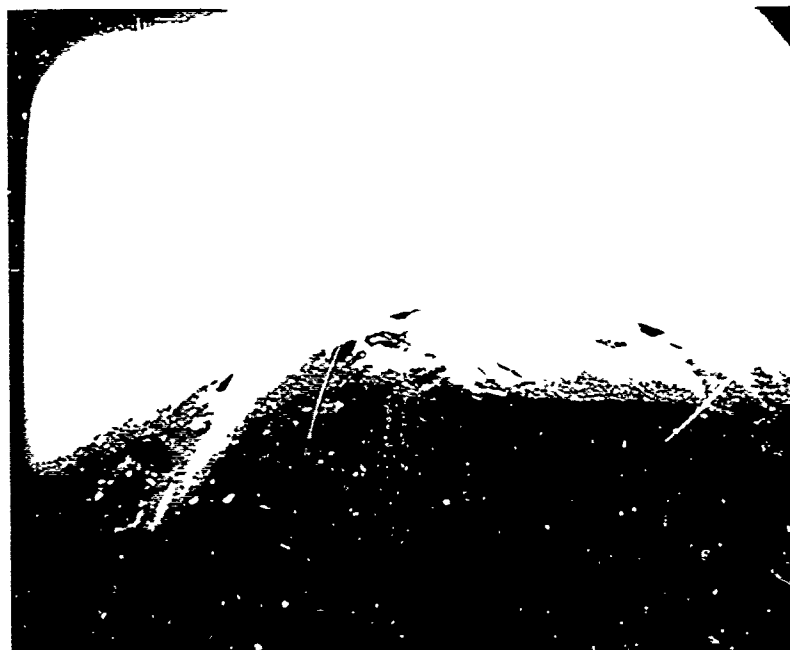
FIGURE 23. Scanning Electron Micrograph of Diamond Point
After 45 Cuts, .002" Depth of Cut on AD 99.5
and High Speed (12,000 rpm). Top 500X Side View,
Bottom 500X Top View.

evidence of crater wear but flats have developed predominantly along

edges 180° apart. Absence of cratering may be due to the low forces

generated at these speeds and the edges may be the surfaces of contact

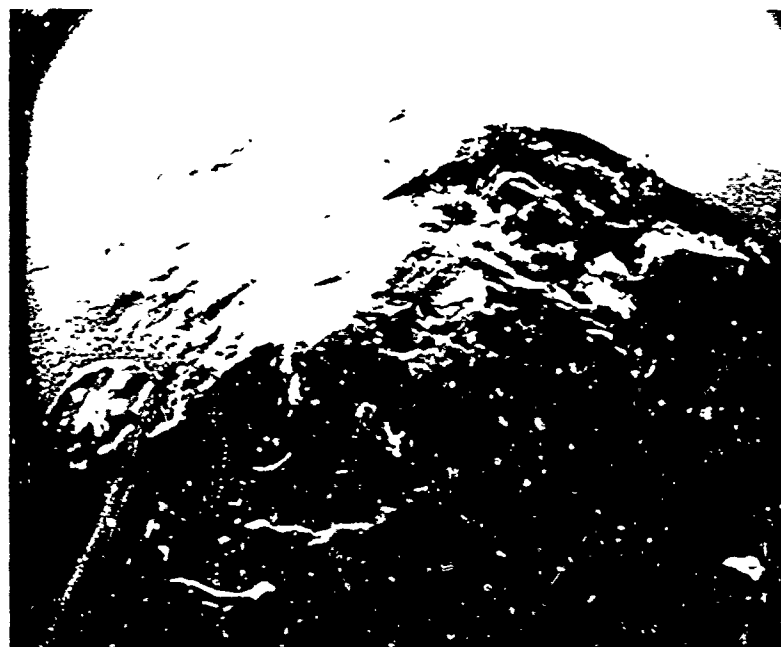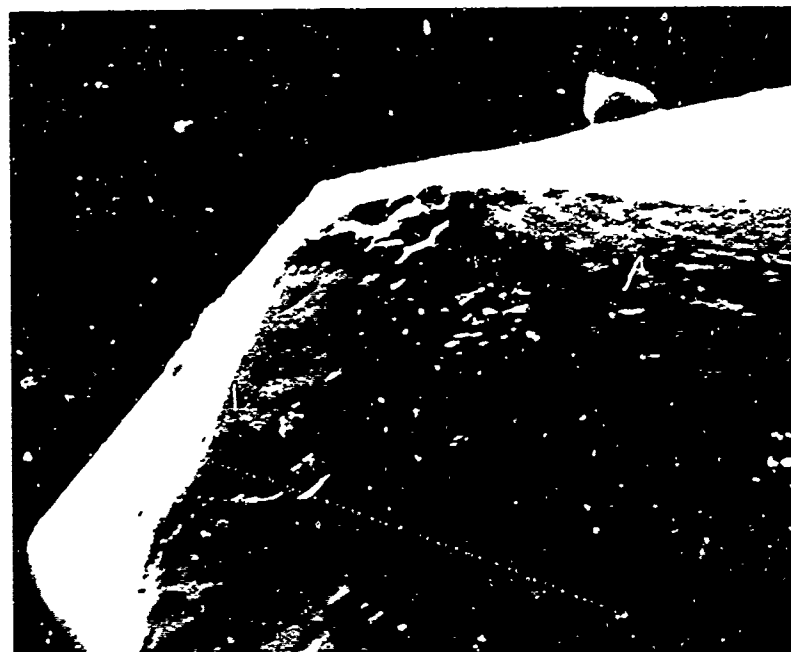of the point with the sides of the groove. Whether this behavior is

characteristic of the higher speed regime needs further verification.

The forces generated with this point increases two-fold after 45 cuts.

With regard to the contention that most (cratering) wear

occurs on the leading edge or impact side of the diamond, the following

is of interest. After making 50 cuts with a point that showed a significant

increase in force, it was rotated 90° and another cut made under identical

conditions. The force produced by this cut dropped to almost the new

point value! A possible explanation of this effect may be advanced on the

basis of the diagrammatic sketch of Figure 24. The point wears more on

one side than on the other. When rotated there is still a point on the

diamond although the tip is not the original tip.

Although conclusive evidence must await further experimentation,

it may be said that:

-- Wear occurs in at least one of two ways: a cratering mode and

   gradual wear mode resulting in the development of flats.

-- Grinding forces developed are a very sensitive indicator of wear

   and provide a basis for quantitative analysis of wear.
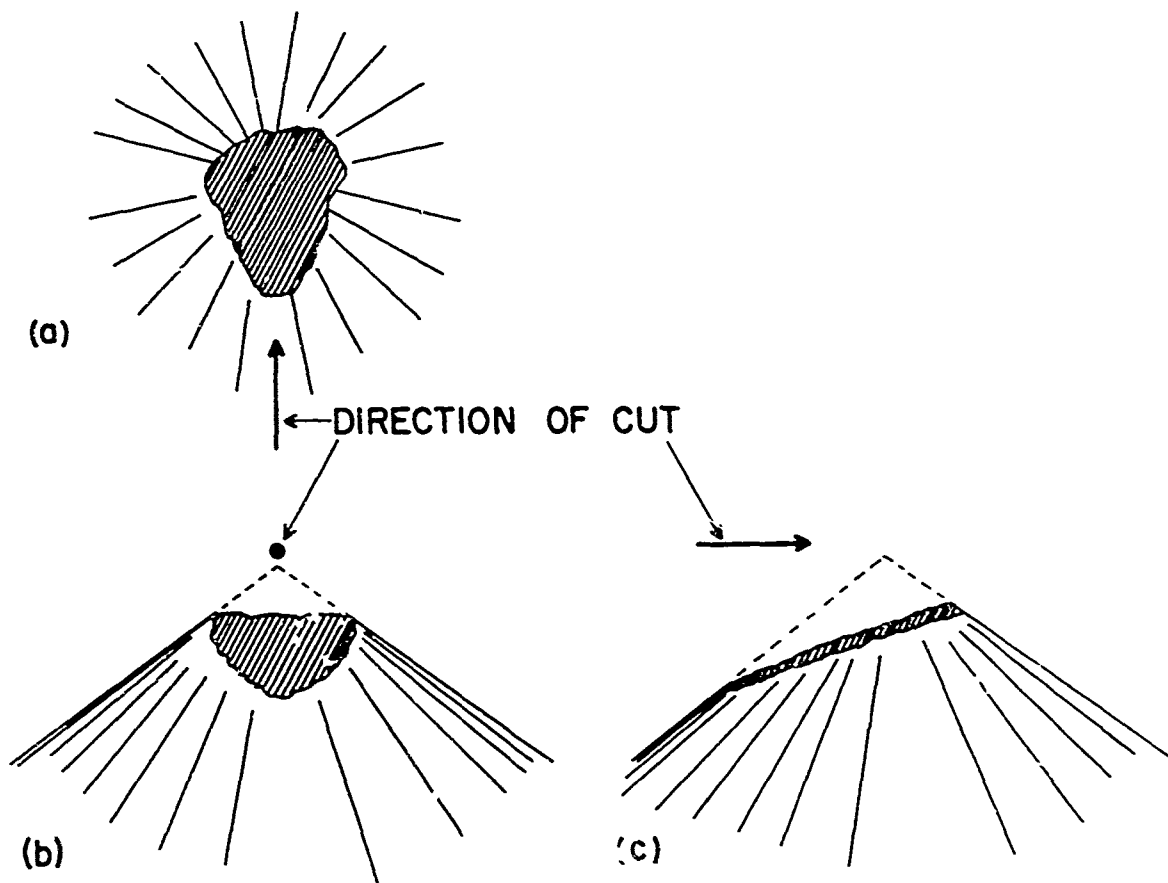
Figure 24. Schematic of Diamond Point Wear Phenomenon
(a) Top View (b) Front View in Cutting Direction
(c) Side View

-- Wear is most pronounced on the leading edge.

-- Wear is definitely related to wheelspeed. The higher the wheelspeed
(at least up to 12,000 rpm, the extent of our measurements) the less
the wear.

From a practical point of view, the above results indicate
that periodic reversal of the wheel, while retaining the direction of
rotation, so as to present the other side of the diamond ("unworn" side)
to the workpiece may have significant effects on grinding efficiency.
This has not been previously proposed and has, to the knowledge of the
investigators, not presently been practiced.

V STOCK REMOVAL MODEL FOR BRITTLE SOLIDS

We have previously introduced an initial dynamic stock removal model which was primarily phenomenologically based. In the following sections we have extended and improved on the phenomenological approach and introduce a more fundamental approach which incorporates material behavior. The latter model, which is to be enlarged upon and will be reported on in the near future, is referred to as the Dynamic-Elastic Model.

A. PHENOMENOLOGICAL MODEL

Consider a diamond point mounted on the periphery of a disk of radius R, revolving at a speed V and cutting into a ceramic workpiece at a depth-of-cut r, while the workpiece is moving with a speed v. The total length of cut across the ceramic will be designated ℓ and the geometric width of the groove W_a. See further Figure 25.

The length of an individual cut (one per revolution) may be expressed as

$$L = (R + r') \theta$$

where θ is the angle of travel during cut of length L.
For $r \ll V$ the individual cut length will be

$$L = \sqrt{2Rr}$$

FIGURE 25. Cutting Wheel and Workpiece Geometry

The total cutting time over the entire length ℓ of th .lock, t, will be,

$$t = \frac{\ell}{v}$$

The time for one revolution, T, is

$$T = \frac{2\pi R}{V}$$

from which follows the number of cuts during passage over the total length, N,

$$N = \frac{V}{2\pi R} \frac{\ell}{v}$$

From strict geometric considerations (see Figure 25) the total volume removed, U_T, will be

$$U_T = \frac{W_a \ell r}{2}$$

from which the volume removed per individual cut, $U_c = U_T/N$ may be obtained,

$$U_c = \frac{\pi W_a R r v}{V}$$

If we make the assumption that the energy expended by the cutting wheel is linearly dependent on the volume of stock removed, then the energy spent per cut, E, can be given by

$$E = c' \pi W_a R r \left(\frac{v}{V} \right)$$

This energy E is spent during traversal of the distance L in time τ where $\tau = L/V$ and c' is a constant. We thus have,

$$E = \int_0^L F \cdot d\ell$$

where F is the instantaneous force. If one makes the assumption that the force F remains a constant during an individual cut and r stays constant as well, the force may be expressed as

$$F = c' \, \Pi \, W_a \, \frac{Rr}{L} \left(\frac{v}{V} \right)$$

or, since $L = \sqrt{2Rr}$, the relative single point force becomes,

$$\boxed{F = c' \, \Pi \, W_a \, \frac{\sqrt{Rr}}{2} \left(\frac{v}{V} \right)}$$

This is substantially the same expression as advanced before,[2] except for the proportionality constant, the value of which most likely will vary from material to material. From a physical point of view, c' lumps all material dependent factors which determine the energy required for fracture.

With the assumptions made, energy linearly dependent on volume removed and F and r constant during the individual cut, the diamond will experience a periodic stress as shown in Figure 26. It must be emphasized here that this is only the gross feature of the periodic stress and wide variations in the transient stress can be expected as will be discussed later. These variations from transient stress can be expected as a result of:

-- the nature of the stress distribution

-- the nature of the material yield or fracture

   (i.e. non-elastic behavior)

-- further geometric considerations.

Departure from strict square wave behavior as shown in Figure 26 may even be shown from some simple geometric considerations. Consider Figure 27 ACB and A'CB' represent the tracks of two individual successive cuts. The distance δ is given by,

$$\delta = vT = \frac{2\pi Rv}{V}$$

In the foregoing treatment the assumption was made that the depth of cut, r, remained constant during the length of cut. Clearly this assumption is not realistic as Figure 27 shows and from which may be seen that $r = PQ$ is a function of Θ. For $r \ll R$ it can be shown that

$$PQ = r = \delta \sin \Theta = \frac{2\pi Rv}{V} \sin \Theta = \frac{2\pi Rv}{V} \Theta$$

The maximum value of Θ is given by

$$\Theta_m = \frac{V}{R} \tau$$

$$r = \frac{2\pi Rv}{V} \sin \frac{V}{R} \tau$$

We can now express a time dependent single cut force, F_t, as

$$\tau = \frac{2Rr}{V}$$

$$T = \frac{2\Pi R}{V}$$
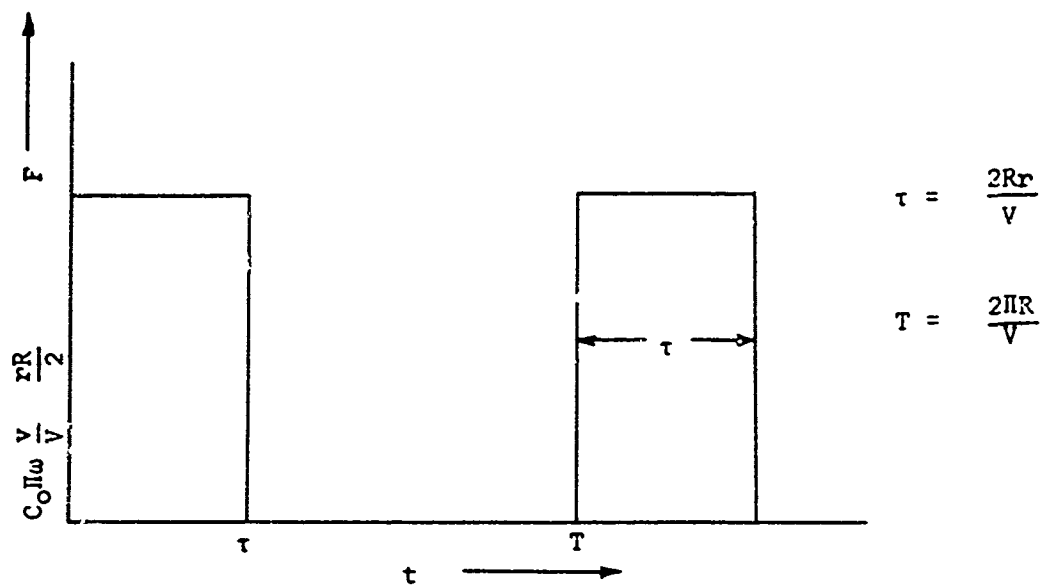
FIGURE 26.   Force Experienced by the Cutting Point.
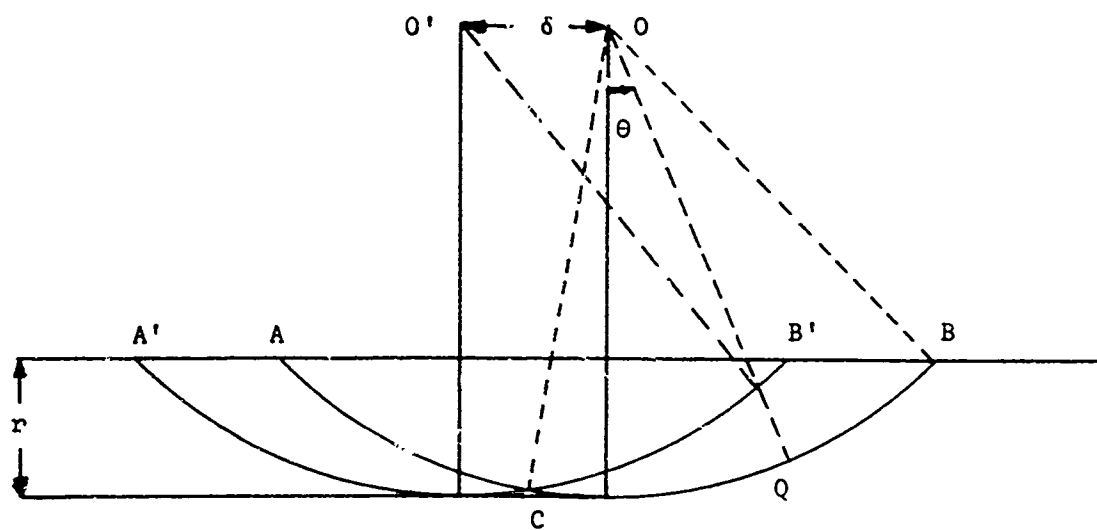
FIGURE 27.   Trajectory of Cutting Point in Two Successive Cuts.

$$F_t = c'' \, \Pi \, W_a \left(\frac{v}{V} \right) \sqrt{\frac{\Pi R^2 v}{V} \sin \frac{V}{R} \tau}, \quad 0 \le t \le$$

which will equal zero for $\tau \le t \le T$.

For small cut approximation we have

$$F_t = c'' \, \Pi \, W_a \frac{v}{V} \sqrt{\Pi v R t}$$

or

$$F_t = c'' \, W_a \frac{(\Pi v)^{3/2}}{V} \sqrt{Rt}$$

The new constant c'' is related to c' by the following relation,

$$\int_0^\tau F \cdot V \, dt = E$$

thus,

$$c'' \, W_a \frac{(\Pi v)^{3/2}}{V} \sqrt{R} \int_0^\tau \sqrt{t} \, V \, dt = c' \, \Pi \, W_a \left(\frac{v}{V} \right) \frac{v \tau}{2}$$

and

$$F_{(t)} = \frac{3c'}{2\tau} \sqrt{\frac{r}{2 \Pi v}} \, W_a \frac{(\Pi v)^{3/2}}{V} \sqrt{Rt}$$

or

$$F_{(t)} = \frac{3c'}{2\tau} \, W_a \, \Pi \left(\frac{v}{V} \right) \sqrt{\frac{Rrt}{2}}$$

where $F_{(t)}$ is the time dependent single cut force and r is the nominal depth of cut.

The stress distribution as a function of time is now changed from strict
square wave behavior to that shown in Figure 28. The assumption is still
that energy is linearly dependent on volume.

The constant c' may also be evaluated. The time average force,
$\overline{F}$, which would be measured by the dynamometer is given by,

$$\overline{F} = c' \; \Pi \; W_a \; (\frac{v}{V}) \; \sqrt{\frac{Rr}{2}} \cdot \frac{\tau}{T}$$

$$= c' \; W_a \; \frac{vr}{2V}$$

from which the constant may be expressed as,

$$c' = \frac{2V\overline{F}}{rvW}$$

The phenomenological hypothesis could be checked out by determining c' for
various values of the systems parameters contained in the expression.

It is important to point out that the force expressions derived
in this pehnomenological model cannot be expected to validly represent the
stress induced in the ceramic. The stress will distribute itself into the
entire body of the ceramic with the stress distribution pattern depending
on many factors, none of which have been taken into consideration so far.
They will be discussed in the next subsection. With regard to the stresses
being induced in the diamond the use of the expressions given above is far
better justified. The diamond is a small system (compared to the ceramic
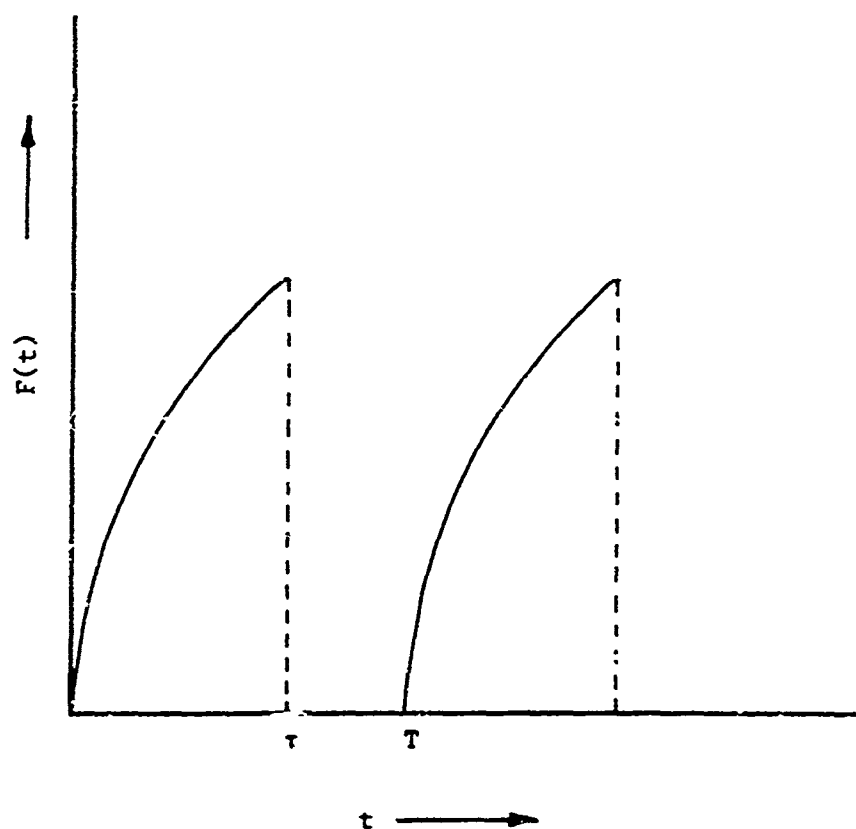block) and the stress can distribute itself over a time much smaller than τ.

FIGURE 28.   Force Experienced by Cutting Point
             as Corrected for Geometrical Fac\ s.

The phenomenological model cannot adequately describe the fracture phenomenon per se since that depends essentially on instantaneous stress distribution. It will entail incorporating the elastic properties of the ceramic. A dynamic-elastic model is advanced below.

B. DYNAMIC-ELASTIC MODEL

The shaded area of Figure 29 represents a typical cut made in a single pass by the diamond cutting point. Components H and V measure the horizontal and vertical forces. A simple geometrical examination of the cutting point D at a typical angle O reveals that the velocity of D has a large H component (θ is always ~ 0) and a small V component (vertically downward is positive). Thus one expects that horizontal forces parallel to the surface, i.e. shear phenomena, would play a more significant role than the compressive phenomena associated with the normal component. It is implied that V, if measured experimentally, would be very small and negative. Instead, what we observe is the application of a smal. V component. The question of what one measures at H and V will be discussed separately. In the model proposed here, the effect of normal component (V) on the stress will be neglected as a first approximation.

As a first step we shall consider the ideal case of a point shear stress, P. applied to a thin infinite slab at its surface defined by y = 0 (See Figure 30). It can be shown[3] that the stress at any point

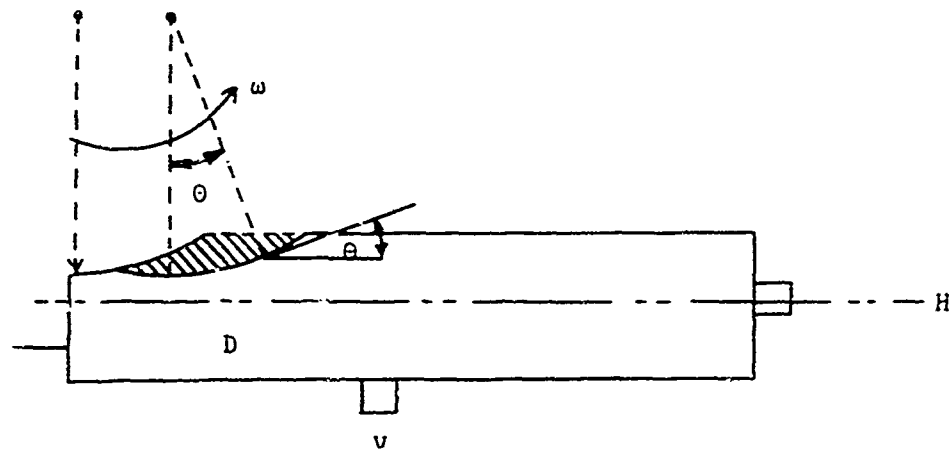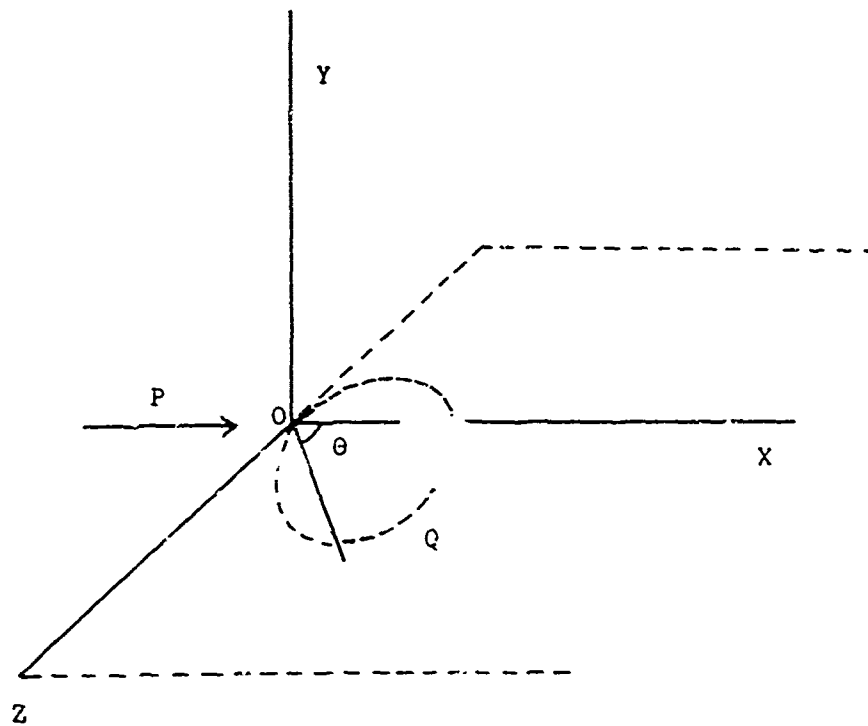FIGURE 29. Geometrical Configuration of Force Measurement Experiment.

FIGURE 30. Two Dimensional Statis Stress Distribution.

$$Q(r,\Theta) \quad (r = \sqrt{x^2 + z^2}, \quad \tan \Theta = X/Z)$$

is purely radial compression and is given by

$$\sigma_r \ (r,0) = - \frac{2P}{\Pi} \cdot \frac{\text{Cos}\Theta}{r} \tag{1}$$

Equation (1) is based on the following normalization:

$$\oint_c \sigma_r \ rd\Theta = P \tag{2}$$

where c is the circle of radius rsecΘ and whose tangent at the origin is the Z-axis. For the three dimensional generalization of (1) we would assume a Rayleigh behavior which will be justified later. Thus,

$$\sigma_v \ (r,\Theta,y) = - \frac{2P'}{\Pi} \ \frac{\text{Cos}\Theta}{r} \ e^{-\beta y} \tag{3}$$

The constant β can be determined by theory of elasticity as will be done subsequently and P' is determined by three dimensional generalization of (2) such that the line integral is replaced by a surface integral such that

$$\int_j \vec{\sigma} \cdot \vec{ds} = P \tag{4}$$

Of course the stress distribution is not purely compressional and shear stresses, which depend on β exist inside the material.

Both Equation (1) and (3) describe the static stress distributions when the entire system is under equillibrium. However, for stock removal processes it is important to analyze the dynamics of stress propagation preceeding the static stress distribution, i.e. one must investigate the problem from a dynamic elasticity point of view. In this context the mathematical idealization of the problem can be formulated as follows: Point 0 in Figure 31 is given a constant velocity v in the x-direction, calculate the general space-time stress function. Once the stress distribution is calculated we would investigate the possibility, location, and the extent of fracture under such a stress field. One might remark at this point that this problem is significantly different from the more widely studied problem of armour failure[4] under ballistic impact or micro-meteorite penetration of astronautical systems. In these processes failure occurs under compressive dynamic load whereas for stock removal (as discussed earlier) shear stress should play the major role. We shall first consider the simpler one-dimensional analogue[5] of this problem.

In Figure 32 a semi-infinite rod (of density ρ, Young's Modulus E), along the x-axis, is driven by D at $x = 0$ by a constant velocity v. It can be shown that the space time stress distribution is given by

$$\sigma (x,t) = \frac{vE}{C} S(ct-x) \tag{3}$$
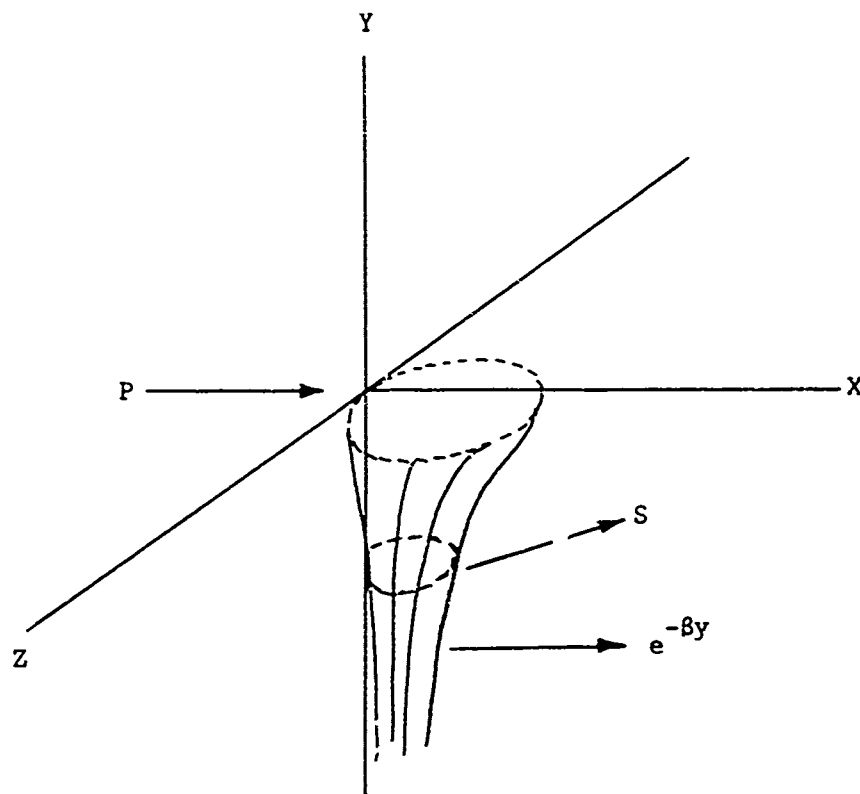
where $S(y)$ is the Heaviside step function such that

FIGURE 31. Three Dimensional Stress Distribution
Due to Localized Shear Loading.
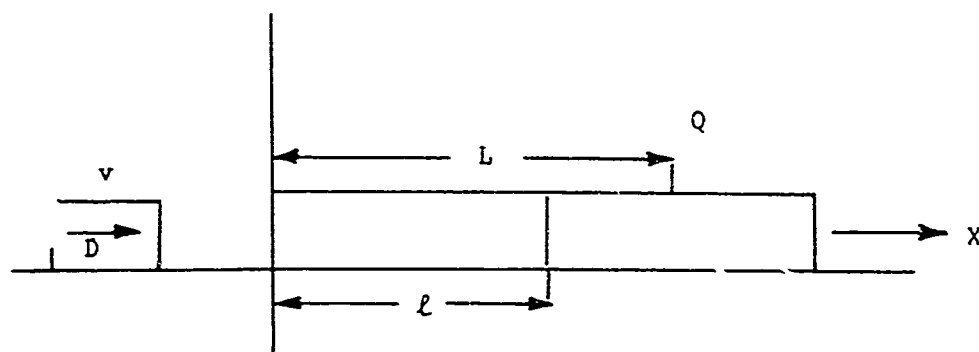

FIGURE 32. One Dimensional Model.

$$S(y) = 1 \qquad\qquad y \geq 0$$
$$S(y) = 0 \qquad\qquad y \leq 0 \qquad\qquad (6)$$

and

$$C = \sqrt{E/\rho} \qquad\qquad (7)$$

Note that since it is a one dimensional problem only the Young's Modulus has to be considered.

The total energy spent by the driving mechanism up to any instant t is given by

$$E(t) = \frac{1}{2} \left[ct\rho v^2 + \frac{ct\sigma^2}{E} \right] + \text{Internal Friction} \qquad\qquad (8)$$

The first term is the kinetic energy of the strained part, the second one gives the strain energy of deformation. The last term is self explanatory. If internal friction is neglected, as we shall do for a first approximation, then it can be shown that[6]

$$ct\rho v^2 = \frac{ct\sigma^2}{E} \qquad\qquad (9)$$

and thus

$$E(t) = ct\rho v^2 = \frac{ct\sigma^2}{E} \qquad\qquad (10)$$

From this one could calculate that the force F_D applied by the driver is

$$F_D = \frac{dE}{dX} = \frac{dE}{dt}\frac{dt}{dX} = \rho v^2 \frac{\sigma^2}{E} \qquad\qquad (11)$$

Now let us consider the force, F_Q, measured by a transducer Q (Figure 32) at a distance L from the origin and compare this with the force F_D experienced by the driver. We expect the time dependence as shown in Figure 33. The area under these curves is proportional to the total energy spent by D.

If there exists a crack at a length ℓ and if the stress σ as given by (5) is large enough (i.e. larger than the critical stress by e.g. the Griffith theory)[7] the rod will fracture at ℓ. Assuming that the fracture takes place simultaneously with the arrival of the elastic wave, then the entire energy $E(t = \frac{1}{c})$ spent will be given to the fracture fragment, i.e. the section of the rod between x = 0 and 1. This energy is proportional to the shaded region in Figure 34 and the force curve would commence at point B instead of A. Thus any attempt made to determine the fracture energy by just measuring the magnitude of force at Q (the transducer) would fail because it would reveal itself purely as a time shift which is very hard to ascertain in a practical situation. Immediately after the fracture, stresses in both D and the rod will be relaxed and F_D, the force on the diamond, would behave as shown in Figure 35. This implies that at $t = \frac{1}{c}$ (due to fracture at x = 1) there is relaxation of stress and thus the force at D falls to zero until D reaches x = 1 the fracture location (at $t = \frac{1}{v}$), moves essentially in the fracture field which offers no resistance.
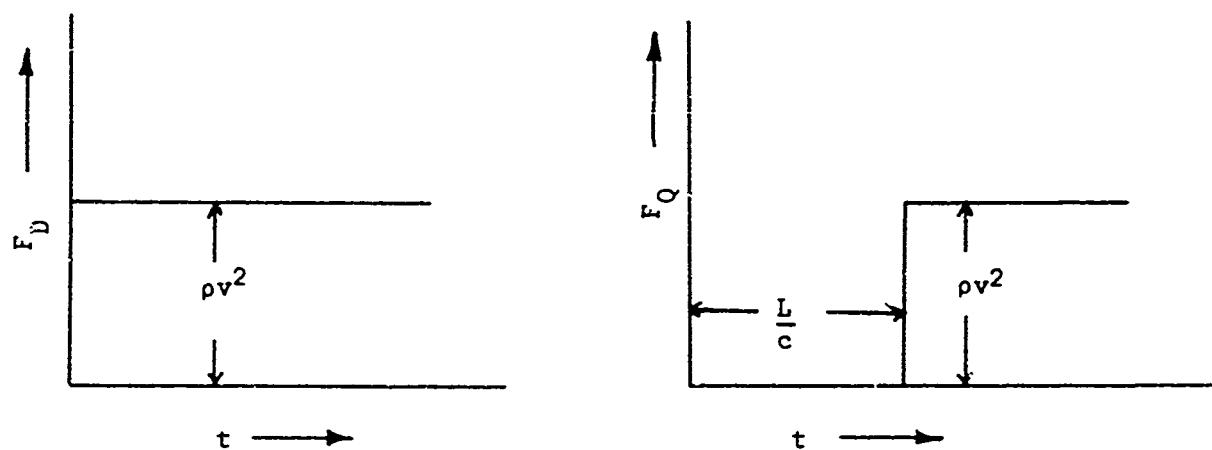
FIGURE 33. (a) Force Experienced by Cutting Point.
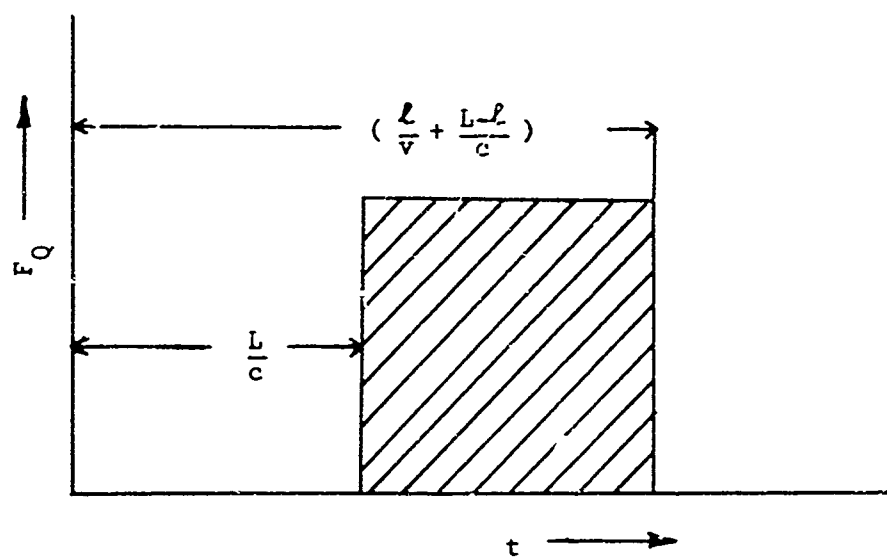(b) Force Measured by Transducer.

FIGURE 34. Force Measured by the Transducer as Modified by a Fracture.

Now let us assume that there are n cracks per unit length (distributed uniformly along x-axis) of the rod, then the force F_D would behave as shown in Figure 36. F_D as measured at D would be a time average force $\overline{F}_D$ where

$$\overline{F}_D = \frac{\rho v^2 \ (1/nc)}{(1/nc + 1/n)} = \frac{\rho v^3}{n(c + v)}$$

$$= F_D \cdot \frac{v}{n(c + v)} \tag{12}$$

According to Griffith's theory a crack of length λ_0 will not propagate until a critical stress σ_0 is reached where,

$$\sigma_0^2 = \frac{\gamma E}{\lambda_0} \tag{13}$$

where λ is surface energy. Combining Equations (5) and (13) and dropping the time dependence, we get

$$\lambda_0 = \frac{\gamma c^2}{E v^2} \tag{14}$$

Equation (14) should be interpreted to imply that at an impact of velocity v, all the cracks of length λ, such that $\lambda_0 < \lambda < \infty$ will propagate. Let $f(\lambda)$ be the statistical distribution function of crack lengths and n_0 the total number of cracks per unit length such that,

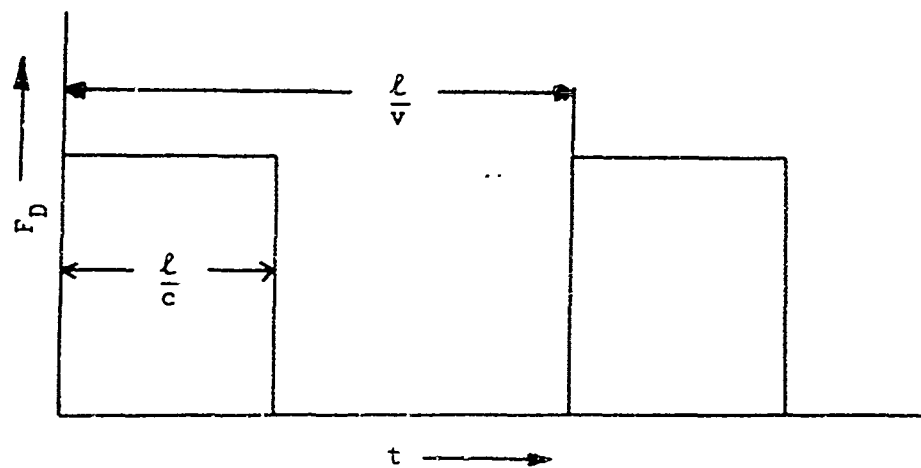$$dn = n_0 \ f(\lambda) \ d\lambda \tag{15}$$

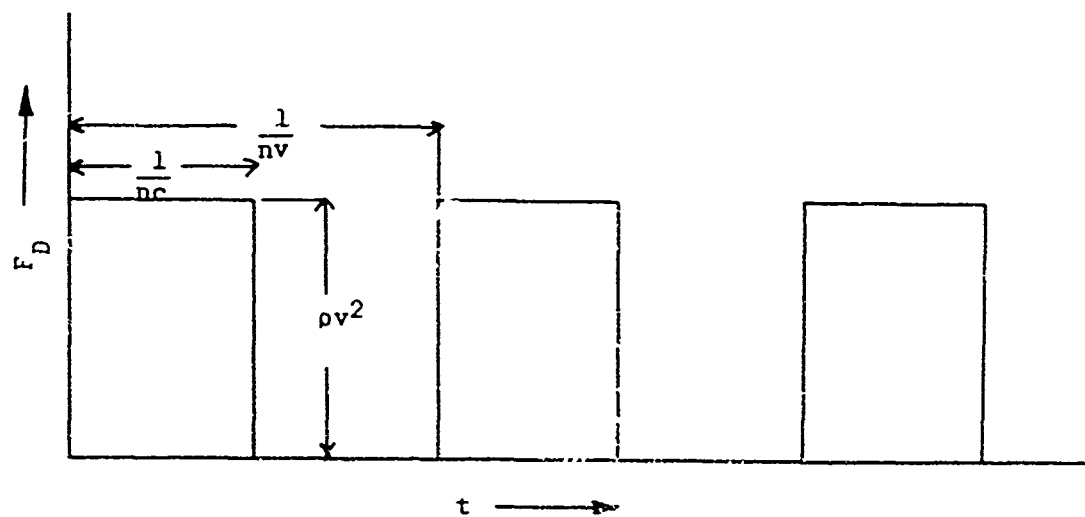FIGURE 35. Force Experienced by Cutting Point as Modified by a Fracture

FIGURE 36. Force Experienced by the Cutting Point as Modified by
a Uniform Periodic Distribution of Cracks.

where n is the number of cracks whose lengths lie in the interval λ and $\lambda+d\lambda$. Thus the total number of cracks per unit length, n, that will propagate by an impact of velocity v is,

$$n = n_0 \int_{\lambda_0}^{\infty} f(\lambda) \, d\lambda$$

and thus Equation (12) becomes

$$\overline{F}_D = F_D \, \frac{v}{n_0(c+v) \int_{\lambda_0}^{\infty} f(\lambda) \, d\lambda}$$

We can now investigate the dependence of force $\overline{F}_D$ on the driver speed v, as shown in Figure 37. At very low speed there is no fracture, provided we assume that very large cracks do not exist, and thus at low speeds the rod will just be indefinitely compressed. We have to assume, of course, that the rod is infinitely long. This behavior is described by curve OA and expressed by ρv^2. At a velocity v_0, the first stress becomes critical for the largest cracks and $\overline{F}_D$ would immediately drop to B by a factor $v/n(c+v)$, see Equation (12). Beyond point B the $\overline{F}_D$ vs v curve will strongly depend on n a' hown in Equation (17). To illustrate this point we will have to assume a. ical form `(λ) the distribution of crack lengths. For the sake of mathematical simplicity we assume a simple, one parameter, parabolic distribution as shown in Figure 33 where λ_0 is the maximum crack length. This gives,
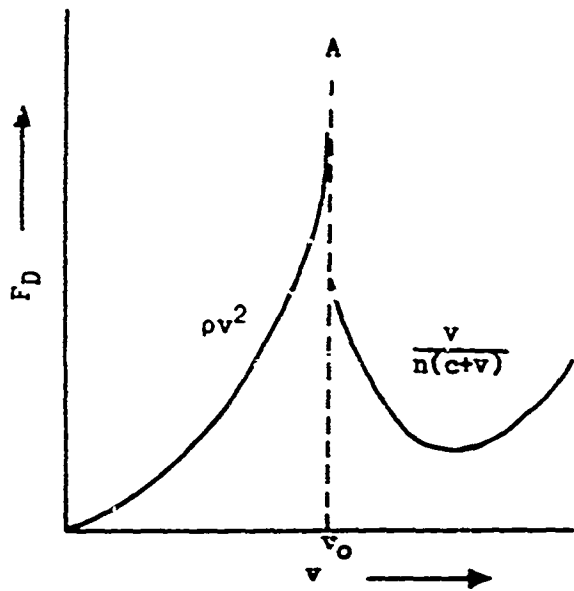
$$f(\lambda) = \lambda_*\lambda_0 - \lambda) \tag{18}$$

FIGURE 37. General Features of $\tilde{F}_D$ in a Brittle Material.
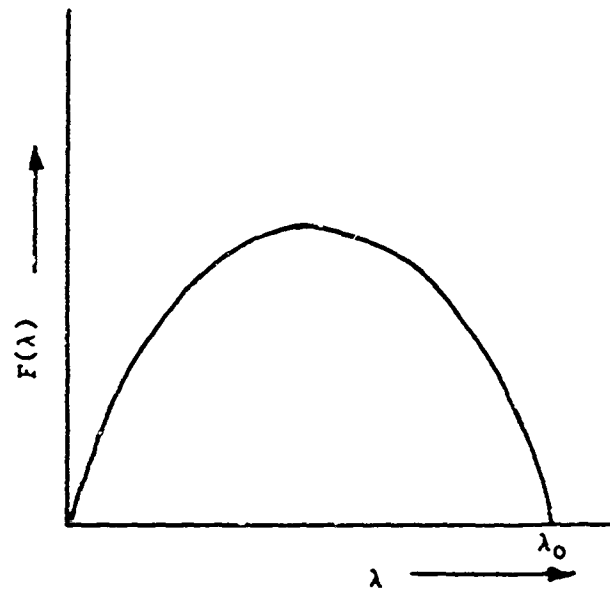
FIGURE 38. Assumed Distribution of Crack Length.
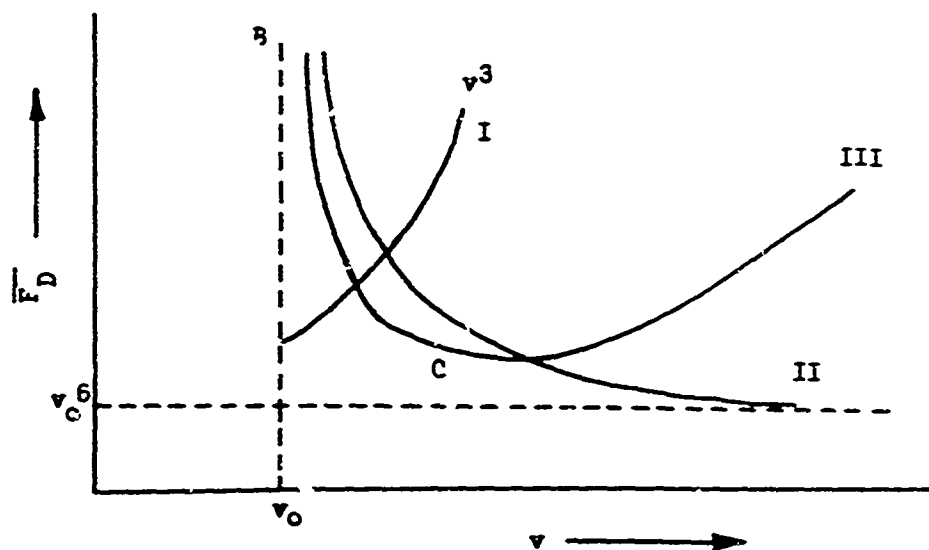
FIGURE 39. Dependence of $\overline{F}_D$ for a Parabolic Crack Length Distribution.

where,

$$\lambda_o = \frac{vc^2}{E\lambda^2} \tag{19}$$

Normalization of this function (18), is left arbitrary.

The number of cracks to be propagated, $n(v)$, at a velocity $v > v_o$ is now given by,

$$n(v) = n_o \int_\lambda^{\lambda_o} f(\lambda) \, d\lambda$$

$$= \frac{n_o}{6} (2\lambda^3 - 3\lambda^2 \lambda_o + \lambda_o^3) \tag{20}$$

In velocity space this becomes,

$$n(v) = \frac{n_o \gamma^3 C^6}{6E^3} \left[\frac{2}{v^6} - \frac{3}{v^4 v_o^2} + \frac{1}{v_o^6} \right] \tag{21}$$

such that (17) can now be written as,

$$\overline{F}_D = \frac{6\rho v^3 E^3}{n_o(c+v) \gamma^3 C^6 \left[\frac{2}{v^6} - \frac{3}{v_o^2 v^4} + \frac{1}{v_o^6} \right]} \tag{22}$$

The v-dependence is determined by the following factors,

$$F_D \sim \frac{v^3}{(c+v)} \cdot \frac{1}{\left[\frac{2}{v^6} - \frac{3}{v_o^2 v^4} + \frac{1}{v_o^6} \right]} \tag{23}$$

The first factor for $c \gg v$ increases approximately as v^3. The second factor to be called [II] has the following behavior for $v_0 < v < \infty$,

$$\underset{v \to v_0}{L_t} [\text{ II }] \to \infty$$

$$\underset{v \to \infty}{L_t} [\text{ II }] \to v_0^6$$

as shown in Figure 39.

Since at $v \sim v_0$, [II] decreases as v^6 whereas the first factor increases only as v^3, the overall term decreases as $\sim v^3$ as shown by BC of curve III in Figures 37 and 39.

Curve III is thus the summation of curves I and II and clearly forms the basis for our experimental findings (Section I) that forces as a function of wheelspeed initially decrease sharply, go through a minimum and continue to rise beyond this. There is thus a sound theoretical argument to be used for the experimental data. One can explicitly calculate the minima of force by considering the factor

$$\tilde{F}_D \sim \frac{v^3}{\left[\dfrac{2}{v^6} - \dfrac{3}{v_0^2 v^4} + \dfrac{1}{v_0^6} \right]}$$

which can be written as

$$\overline{F}_D \sim \frac{v^9}{[\ 2\ -\ 3v^2\ +\ v^6\ ]} \tag{24}$$

where v is now measured in units of v_o, i.e. we have put $v_o = 1$. We now have to find the minima of $\overline{F}_D$ in the range $1 < v < \infty$.

Thus

$$\frac{d\overline{F}_D}{dv}\ =\ 0\ =\ \frac{9v^8}{[\ 2\ -\ 3v^2\ +\ v^6\ ]}\ -\ \frac{v^9\ [\ 6v^5\ -\ 6v\ ]}{[\ 2\ -\ 3v^2\ +\ v^6\ ]}$$

or

$$v^6\ -\ 7v^2\ +\ 6\ =\ 0 \tag{25}$$

To find the roots of Equation (25) we put,

$$v^2 = 7$$

and thus,

$$y^3\ -\ 7y\ +\ 6\ =\ 0 \tag{26}$$

which can be written as,

$$(y-1)\ (y-2)\ (y+3)\ =\ 0 \tag{2..}$$

where $y = 1$, and -3 are nonintersecting roots and $y = 2$ gives $v = \pm\ \sqrt{2}$. Thus at,

$$v\ =\ \sqrt{2}\ v_o \tag{28}$$

$\overline{F}_D$ will be a minimum. The minimum in the experimental data curves thus has a distinct physical significance. Since v_o, the speed at which the stress becomes critical, will be dependent on the material parameters, the minimum will be material dependent as we have indicated previously from experimental data.[2] A shift of the minimum towards higher speeds will be observed for higher strength materials. The above is of course based on the assumption that the crack length distribution is a parabolic function [Equation (18)] whereas in actual practice it is perhaps more likely to be a Gaussian function[8] which involves even higher powers of λ and would thus make part BC of curve III in Figure 39 even steeper. The minima would occur at some point other than that given by Equation (28).

Up to now we have considered the average force experienced by the driver only. The force measured by Q, strictly speaking, should be zero because of the following conditions:

-- One dimensional constraint.[9]

-- Crack propagation and stress relaxation

accomplished simultaneously and in zero time.

If either of the above conditions is relaxed, then $\overline{F}_Q \neq 0$. We shall first consider the relaxation of the second condition. This is certainly justifiable on purely physical grounds since both crack propagation and stress relaxation require finite time as can be expected by dynamic generalization of Hookes law through the introduction of Maxwell, Voigt or some other similar mechanism. The relaxation process and therefore

the relaxation time is a complicated function of various systems parameters. However, to illustrate the model, we assume a constant relaxation time, τ, such that during this time the crack propagates and the elastic wave continues to travel as if no stress relaxation has taken place. Furthermore, to avoid interference between two successive fractures it is assumed that $\tau < \frac{1}{nv}$. This assumption can be put in an alternate way. The elastic wave passing through a propagating crack is reduced in intensity so that it will not start new crack propagation.

The mathematical essence of all these assumptions is that the elastic wave passing through the propagating crack is of a duration τ and height proportional to F_D. Thus the only mathematical statement that can be made regarding F_Q is that it will be proportional to F_D and thus apart from a normalization constant, $\overline{F}_Q$ will be given by Equation (17) and behave as shown in Figure 39.

VI CONCLUSIONS

The results of our high speed single point cutting tests have significantly added to an understanding of the ceramic grinding process. The importance of wheelspeed is paramount. It governs the actual amount of material removed per unit input energy primarily because of its influence on the extent of breakup and subsequent removal of material in bo h depth and width. It is significant to note that increased wheelspeed not only promotes a significantly higher stockremoval rate but imparts a reduction in cutting force while at the same time drastically reducing wear on the diamond. There are further implications with regard to the design of grinding wheels for optimum stockremoval practice. Present practice seems to act counter to the beneficial factors shown to be available if proper use were made of the influence of size, geometry, concentration strength of diamond and abrasive distribution in the wheel. It appears that materials other than diamond could be efficiently applied in stockremoval practice on ceramics, provided the proper systems parameters were selected.

Scanning Electron Microscopy has shown that diamond wear occurs in one of two ways: cratering or bulk removal of diamond as a result of the impact forces and gradual wear resulting in the so-called wear flats. Wear is directly related to an increase in the grinding force. The, so far, linear relationship between increase in grinding force and extent

of wear has been established through the use of a high frequency response piezoelectric dynamometer. Amount of wear, so far determined under dry conditions only, is critically influenced by the physical characteristics of the workpiece. The harder, denser, higher alumina content workpieces affect higher wear rates. Distinction between wear rates on different types of aluminas is discreet. Increasing diamond life on high wear type workpieces will and can be accomplished by choosing conditions which minimize the actual forces experienced by the diamond in the cutting operation. As our experiments indicate, this can be done through adjusting either machine, wheel or workpiece parameters, a combination of the above or preferably all.

The phenomenological grinding model presented here clearly shows the influence of the more important and adjustable parameters on force level and removal rate. It offers however little information on the critical role played by the physical characteristics of the workpiece nor can it quantitatively distinguish between them. Our initial dynamic-elastic model on the other hand does take these factors into account and had successfully explained the course of grinding forces with varying wheelspeed. It further makes possible the a priori determination of grinding forces and energies from one ceramic material to another and thus enables evaluation of wear and performance to be expected.

Several of the topics discussed in this report need further evalu·tion and extension. Beyond that there seems to be particular need .ᵗ verify the concepts which have so far resulted from more basic or fundamental type investigations. There seems little doubt that reductiᵥᶰ to practice, at least as far as feasibility is concerned, should be includeᵤ and should result in significant advances in future stockremoval systems for application in ceramic technology.

REFERENCES

1. P. J. Gielisse and J. Stanislao. Material Removal Phenomena in Ceramics. First Annual Report, Contract #N00019-69-C-0131, Naval Air Systems Command, December 1969.

2. P. J. Gielisse and J. Stanislao. Dynamic and Thermal Aspects of Ceramic Processing. Final Technical Report, Contract #N00019-70-0163, Naval Air Systems Command, December 1970.

3. Timoshenko and Goodier. Theory of Elasticity. New York: McGraw Hill, 1956.

4. M. L. Wilkins, et al. UCRL 50694.

5. B. Steverding. J. Am. Cer. Soc., 52, No. 3, 13 (1968).

6. H. Kolsky. Stress Waves in Solids. New York: Dover Publications, Inc., 1963.

7. A. A. Griffith. Proc. Intern. Congr. on Appl. Mech., Delft, 1924.

8. E. E. Underwood, et al. Ceramic Microstructure. ed. Fulrath and Pask. Proc. III, Berkeley Int. Mat. Conf., June 13-16, 1966, John Wiley and Son.

9. L. A. Galin. Contact Problems in the Theory of Elasticity, ed. I. N. Snedden Dept. of Math., North Carolina State College, Raleigh, 1961.